Mon. Not. R. Astron. Soc. **000**, 1–20 (2016) Printed 26 July 2016 (MN LATEX style file v1.4)

# No Signatures of Black-Hole Spin in the X-ray Spectrum of the Seyfert 1 Galaxy Fairall 9

T. Yaqoob[1,2], T. J. Turner[2], M. M. Tatum[2], M. Trevor[2], A. Scholtes[2]
[1] *Department of Physics and Astronomy, Johns Hopkins University, 3400 N. Charles St., Baltimore, MD 21218.*
[2] *Department of Physics, University of Maryland Baltimore County, Baltimore, MD 21250.*

arXiv:1607.07125v1 [astro-ph.HE] 25 Jul 2016

Received

**ABSTRACT**

Fairall 9 is one of several type 1 active galactic nuclei for which it has been claimed that the angular momentum (or spin) of the supermassive black hole can be robustly measured, using the Fe K$\alpha$ emission line and Compton-reflection continuum in the X-ray spectrum. The method rests upon the interpretation of the Fe K$\alpha$ line profile and associated Compton-reflection continuum in terms of relativistic broadening in the strong gravity regime in the innermost regions of an accretion disc, within a few gravitational radii of the black hole. Here, we re-examine a *Suzaku* X-ray spectrum of Fairall 9 and show that a face-on toroidal X-ray reprocessor model involving only nonrelativistic and mundane physics provides an excellent fit to the data. The Fe K$\alpha$ line emission and Compton reflection continuum are calculated self-consistently, the iron abundance is solar, and an equatorial column density of $\sim 10^{24}$ cm$^{-2}$ is inferred. In this scenario, neither the Fe K$\alpha$ line, nor the Compton-reflection continuum provide any information on the black-hole spin. Whereas previous analyses have assumed an infinite column density for the distant-matter reprocessor, the shape of the reflection spectrum from matter with a finite column density eliminates the need for a relativistically broadened Fe K$\alpha$ line. We find a 90 per cent confidence range in the Fe K$\alpha$ line FWHM of 1895–6205 km s$^{-1}$, corresponding to a distance of $\sim 3100$ to $33,380$ gravitational radii from the black hole, or 0.015–0.49 pc for a black-hole mass of $\sim 1-3\times10^8\ M_\odot$.

**Key words:** black hole physics - galaxies: active - galaxies: individual (Fairall 9) - radiation mechanism: general - scattering

## 1 INTRODUCTION

Fairall 9 is a bright, nearby ($z = 0.047016$) Seyfert 1 galaxy that has been the subject of several studies that attempt, using X-ray spectroscopy, to obtain robust measurements of the angular momentum, or spin, of the putative supermassive central black hole (Schmoll et al. 2009; Emmanoulopoulos et al. 2011; Patrick et al. 2011a, 2011b, 2013; Lohfink et al. 2012a; Walton et al. 2013; Lohfink et al. 2016). According to the "no hair" theorem, black holes have only three measurable physical attributes, one of these being spin (mass and charge being the other two). In addition to its importance for fundamental physics, black-hole spin affects the energetics and evolution of the environment in which the black hole resides. Thus, the spin properties of black holes in a population of sources, such as active galactic nuclei (AGN), could provide clues pertaining to the formation and growth of supermassive black holes (e.g. see Volonteri & Begelman 2010).

The reason why Fairall 9 has been of particular interest for black-hole spin measurements via X-ray spectroscopy is that it is a member of a subset of AGN that have been established to exhibit few or no signatures of line-of-sight absorption that could complicate modeling of the X-ray spectral features that are thought to carry signatures of black-hole spin (Gondoin et al. 2001; Emmanoulopoulos et al. 2011). Otherwise known as "bare Seyfert galaxies", AGN such as Fairall 9 provide a "clean" direct view of the accreting black-hole system (e.g. Patrick et al. 2011a; Tatum et al. 2012; Walton et al. 2013). It is the X-ray spectrum from the innermost regions of the accretion disc that is thought to convey the signatures of relativistic effects in the

© 2016 RAS

vicinity of the black hole, including its spin. The basic method for constraining the black-hole spin involves fitting a model of the X-ray reflection spectrum from the accretion disc, and the associated Fe K$\alpha$ emission line, with the broadening, or "blurring" effects of Doppler and gravitational energy shifts being the key drivers (e.g., see Reynolds 2014; Middleton 2015, and references therein). The disc-reflection model invariably used in the literature for AGN in general is REFLIONX (Ross, Fabian & Young 1999; Ross & Fabian 2005), combined with one of several alternatives for the "blurring" kernel (e.g. Laor 1991; Dovčiak, Karas & Yaqoob 2004; Brenneman & Reynolds 2006; Dauser et al. 2010). Other model components often need to be included to account for features that may or may not be directly related to the accreting black-hole system (for example, additional or alternative soft X-ray emission, and/or narrow emission lines from distant matter at tens of thousands of gravitational radii from the black hole). Clearly, the fewer the number of model components that are needed, the less ambiguity and/or degeneracy there will be in constraining the black-hole spin. The reason why *Suzaku* spectra for Fairall 9 have received the attention of several studies is that the good energy resolution of the CCD detectors for measuring the crucial Fe K$\alpha$ line profile, combined with the simultaneous sensitive coverage above 10 keV, provides a significant advance over previous capabilities for constraining the X-ray reflection spectrum and fluorescent line emission. Early observations of Fairall 9 with *ASCA* (Reynolds 1997) and *XMM-Newton* (Gondoin et al. 2001; Emmanoulopoulos et al. 2011) lacked the high-energy coverage. Nevertheless, a broad Fe K$\alpha$ line (the principal feature required for constraining black-hole spin) was reported for the *ASCA* observation (Reynolds 1997) and for a 2009 *XMM-Newton* observation (Emmanoulopoulos et al. 2011), but for an earlier *XMM-Newton* observation in 2000, Gondoin et al. (2001) reported no detection of a broad Fe K$\alpha$ line. More recently, Fairall 9 was targeted by a *Swift* monitoring campaign and three new *XMM-Newton* observations, one of them simultaneous with *NuSTAR* (Lohfink et al. 2016). Although it was stated by the authors that they "clearly detect blurred ionised reflection," detection of a relativistically broadened line alone (as opposed to the joint detection of such a line and the reflection continuum as a single spectral component), was not claimed.

The result of all the X-ray spectroscopy studies of Fairall 9 that attempt to measure the black-hole spin is a wide range in its inferred value, ranging from zero to 0.998, the theoretical maximum for accretion (Thorne 1974). Analyses of different data sets, as well as the same data set with different models, yield different black-hole spin measurements, some of which are inconsistent within the given errors. In some cases, the inferred inclination angle of the accretion disc and the iron abundance are also inconsistent amongst different data sets and models applied. Lohfink et al. (2012a) tried to resolve these serious conflicts by adding an additional soft X-ray continuum to their model and forcing the black-spin, disc inclination angle, and iron abundance to be invariant amongst different *XMM-Newton* and *Suzaku* data sets. However, this procedure involved adding nine free parameters in total to an already complex model, so it is not surprising that a consistent value of black-hole spin was able to fit the data. Moreover, Lohfink et al. (2012a) explained that the two different models of the additional soft X-ray continuum both left unresolved problems. In one case the additional soft X-ray continuum was a thermal Comptonisation component that implied a colossal iron overabundance, with a lower limit of 8.2 relative to solar. In the other case, the additional component was an ionised reflection spectrum (using the REFLIONX model), but this solution implied a radial ionisation gradient in the accretion disc that predicts atomic features in the spectrum that are not observed. Even if a viable consistent solution for the black-spin can be found for different data sets, the problem of the model-dependence of the black-hole spin based on fitting the same data with different models still remains. Patrick et al. (2011b) studied this model dependence for a small sample of AGN observed by *Suzaku* (including Fairall 9), and the severity of the model dependence led them to conclude that "zero spin cannot be ruled out at a particularly high confidence level in all objects." The principal difference in the applied models pertained to the exact model used for relativistic broadening of the Fe K$\alpha$ line (including the option of omitting that component altogether). Several choices are available for such a model in popular X-ray spectral-fitting packages (e.g. Dovčiak et al. 2004; Dauser et al. 2010; Patrick et al. 2011a; Middleton 2015).

It is also known that partial covering models can sometimes eliminate the need for a relativistically broadened Fe K$\alpha$ emission line (e.g. Miller, Turner & Reeves 2008; Iso et al. 2016). In such a scenario, there is degeneracy between the spectral curvature due to relativistic broadening of the Fe K$\alpha$ line and the spectral curvature due to absorption by matter that partially covers the X-ray source. However, only one-dimensional partial covering models are typically applied, which may be incomplete because only line-of-sight absorption is considered, and Compton scattering and fluorescent line emission from any globally distributed matter is not included. Recently, a more sophisticated partial covering model has been applied to Mkn 335 (Gallo et al. 2015), but the spectra were so complicated that both the blurred reflection model and the partial covering model left unmodeled residuals. It is therefore important to first understand the much simpler spectra of bare Seyfert galaxies such as Fairall 9. Another type of model that eliminates the need for a relativistically broadened Fe K$\alpha$ line whilst also accounting for matter out of the line of sight invokes a Compton-thick accretion disc wind (Tatum et al. 2012), and has also been successfully applied to Fairall 9. A different study involving a disc wind model, applied to the Narrow Line Seyfert galaxy 1H 0707–495 (Hagino et al. 2016), also led to the conclusion that the X-ray spectrum in this source can be modeled with absorption in the wind rather than invoking relativistic effects in strong gravity to produce a broad Fe K$\alpha$ line. The implication of these studies is that if there is no relativistically broadened Fe K$\alpha$ line emission from the innermost regions of the accretion disc, then there is no signature of black-hole spin in the X-ray spectrum. In this scenario, measurements of

black-hole spin obtained from applying models that do have relativistically broadened Fe K$\alpha$ line emission are then artifacts of incorrect modeling.

One feature that is common to all of the above-mentioned models fitted to the X-ray spectra of Fairall 9 is the method of modeling the narrow core of the Fe K$\alpha$ line, which is ubiquitous in both type 1 and type 2 AGN (e.g. Yaqoob & Padmanabhan 2004; Nandra 2006; Shu, Yaqoob & Wang 2010, 2011; Fukazawa et al. 2011; Ricci et al. 2014). Hereafter, it will be referred to as the distant-matter Fe K$\alpha$ line, since it has a width that is typically less than a few thousand km s$^{-1}$ full width half maximum (FWHM), corresponding to an origin in matter located at tens of thousands of gravitational radii from the black hole. Shu et al. (2011) measured a mean FWHM of $\sim 2000 \pm 160$km s$^{-1}$ from a sample of AGN observed by the *Chandra* high energy grating (HEG). They showed that in some AGN the location of the distant-matter Fe K$\alpha$ line emitter is consistent with the classical broad line region (BLR), yet in other AGN the location is further from the black hole, possibly at the site of a putative obscuring torus structure that is a principal ingredient of AGN unification schemes (e.g., Antonucci 1993; Urry & Padovani 1995). The peak energy of the narrow Fe K$\alpha$ line is tightly distributed around 6.4 keV for both type 1 and type 2 AGN (e.g. Sulentic et al. 1998; Yaqoob & Padmanabhan 2004; Nandra 2006; Shu et al. 2010, 2011), providing a strong observational constraint on the neutrality of the matter producing the line, and any associated Compton-scattered continuum. Any attempt to measure the relativistically broadened Fe K$\alpha$ line in AGN X-ray spectra must properly account for the narrow distant-matter Fe K$\alpha$ line because it can carry a luminosity that is comparable to, or even greater than that in the broad component. The models must also account for the Compton-scattered (reflection) continuum in the matter that produces the narrow Fe K$\alpha$ line. Without exception, the previous studies of Fairall 9 described above all use a model for the narrow Fe K$\alpha$ line and the associated reflection continuum that is based on matter with an infinite column density, a flat (disc) geometry, and an infinite size, with the inclination angle of the disc relative to the observer fixed at an arbitrary value. In some cases the narrow Fe K$\alpha$ line emission and the associated reflection continuum are calculated self-consistently using the model PEXMON (Nandra et al. 2007) or even a second ionised disc-reflection spectrum (e.g. REFLIONX) with the relativistic blurring turned off (e.g. Gallo et al. 2015). In other cases the Fe K$\alpha$ line emission is modeled with a simple Gaussian, the reflection continuum is modeled with PEXRAV (Magdziarz & Zdziarski 1995), and the two components (which are in reality not independent), are given ad hoc (floating) normalizations. In yet another variant, the narrow Fe K$\alpha$ line emission is modeled with a Gaussian component and the associated reflection continuum is completely ignored and omitted (e.g. Patrick et al. 2013). The assumption in the latter scenario is that the narrow Fe K$\alpha$ line core originates in Compton-thin matter and that the reflection continuum from that Compton-thin matter is negligible and can be ignored. However, there is no basis for the omission of the reflection continuum from Compton-thin matter and indeed, it was shown in the case of Mkn 3 that it cannot be neglected (Yaqoob et al. 2015). Moreover, several recent studies have shown that the Compton-scattered continuum from matter with a finite column density is different to that from matter with an infinite column density, and exhibits a rich variation in spectral shape (Murphy & Yaqoob 2009; Ikeda et al. 2009; Yaqoob 2012; Liu & Li 2014; Yaqoob et al. 2015; Furui et al. 2016). The so-called "Compton-hump" (the peak in the reflection spectrum) is no longer located at $\sim 30$ keV but depends on the column density (as well as geometry and inclination angle), and can actually be located below the energy of the core of the Fe K$\alpha$ line for column densities $< 10^{24}$ cm$^{-2}$. The complexity of the reflection continuum from matter with a finite column density can potentially model features that are traditionally interpreted as relativistically broadened Fe K$\alpha$ line emission.

In this paper, we make no assumptions about the column density of the matter producing the narrow Fe K$\alpha$ line in Fairall 9 and use the MYTORUS model of a toroidal X-ray reprocessor (Murphy & Yaqoob 2009) to actually let the data determine the global column density of the reflecting material from spectral fitting. In the MYTORUS model, the Fe K$\alpha$ line shape and flux are calculated self-consistently with respect to the associated reflection continuum. A Compton-thick reflection spectrum similar to that from infinite column density disc-reflection models can be recovered as a limiting case in the MYTORUS model, which is based on a more realistic geometry for the circumnuclear matter than the disc geometry that has has been used in all of the previous studies of Fairall 9 (based on models such as PEXRAV and PEXMON). In type 2 AGN, column densities in the line of sight have been observed over a wide range, from Compton-thin to Compton-thick, with some sources exhibiting transitions between Compton-thin and Compton-thick states (e.g. Matt, Guainazzi & Maiolino 2003; Risaliti et al. 2010, and references therein). It should therefore not be surprising if this range of column densities is also appropriate for the circumnuclear matter in type 1 AGN. We note that from extended *RXTE* monitoring data of Fairall 9, Lohfink et al. (2012b) presented evidence of clumps of matter transiting across the X-ray source that did not completely extinguish the X-ray emission. The column density of the clumps was crudely estimated by Lohfink et al. (2012b) to be "a few $\times 10^{24}$ cm$^{-2}$. However, Markowitz, Krumpe, & Nikutta (2014) pointed out that the *RXTE* monitoring data are also consistent with intrinsic spectral variability, an interpretation also given in later work by Lohfink et al. (2016), based on a *Swift*/*XMM-Newton*/*NuSTAR* campaign on Fairall 9 in 2014.

In this paper we apply the MYTORUS model to *Suzaku* data for Fairall 9. The *Suzaku* data are well-suited for studying the X-ray reprocessor because *Suzaku* provides simultaneous coverage of the critical Fe K band ($\sim 6-8$ keV) with good spectral resolution and throughput (due to the XIS CCD detectors), and of the hard X-ray band above 10 keV with good sensitivity. The simultaneous broadband coverage is important for reconciling the absorbed and reflected continua with the

Fe K$\alpha$ line emission. The scope and intent of the present work was to focus on *Suzaku*/*Chandra* HEG data in the short term and provide a framework and basis for additional studies in the long term, e.g. with *NuSTAR*. We will show that our model, which includes no relativistically broadened Fe K$\alpha$ line or disc reflection, gives an excellent fit to the *Suzaku* data. The X-ray spectrum of Fairall 9, which can be explained by Fe K$\alpha$ line emission and X-ray reflection from the distant matter alone, would then carry no information on black hole spin.

The paper is organized as follows. In §2 we describe the basic data, and reduction procedures. In §3 we describe the analysis strategy, including the procedures for setting up the X-ray reprocessing models for spectral fitting. In §4 we give the detailed results from spectral fitting. In §5 we summarize our results and conclusions.

## 2 *Suzaku* OBSERVATION AND DATA REDUCTION

The present study pertains to an observation of Fairall 9 made by the joint Japan/US X-ray astronomy satellite, *Suzaku* (Mitsuda et al. 2007) on 2007 June 7. *Suzaku* carries four X-ray Imaging Spectrometers (XIS – Koyama et al. 2007) and a collimated Hard X-ray Detector (HXD – Takahashi et al. 2007). Each XIS consists of four CCD detectors at the focal plane of its own thin-foil X-ray telescope (XRT – Serlemitsos et al. 2007), and has a field-of-view (FOV) of $17.8' \times 17.8'$. One of the XIS detectors (XIS1) is back-side illuminated (BI) and the other three (XIS0, XIS2, and XIS3) are front-side illuminated (FI). The bandpass of the FI detectors is $\sim 0.4-12$ keV and $\sim 0.2-12$ keV for the BI detector. The useful bandpass depends on the signal-to-noise ratio of the background-subtracted source data since the effective area is significantly diminished at the extreme ends of the operational bandpasses. Although the BI CCD has higher effective area at low energies, the background level across the entire bandpass is higher compared to the FI CCDs. The HXD consists of two non-imaging instruments (the PIN and GSO – see Takahashi et al. 2007) with a combined bandpass of $\sim 10-600$ keV. Both of the HXD instruments are background-limited, more so the GSO, which has a smaller effective area than the PIN. For AGNs, the source count rate is typically much less than the background and in the present study we used only the PIN data, as the GSO data did not provide a reliable spectrum. In order to obtain a background-subtracted spectrum, the background spectrum must be modeled as a function of energy and time. The background model for the HXD/PIN has an advertised systematic uncertainty of 1.3 per cent [1]. However, the signal is background-dominated, and the source count rate may be a small fraction of the background count rate, so the net systematic error in the background-subtracted spectra could be significant. The observation of Fairall 9 was optimized for the XIS in terms of positioning the source at the aim point for the XIS (the so-called "XIS-nominal pointing"), at the expense of $\sim 10$ per cent lower HXD effective area.

The principal data selection and screening criteria for the XIS were the selection of only *ASCA* grades 0, 2, 3, 4, and 6, the removal of flickering pixels with the FTOOL `cleansis`, and exclusion of data taken during satellite passages through the South Atlantic Anomaly (SAA), as well as for time intervals less than 256 s after passages through the SAA, using the T_SAA_HXD house-keeping parameter. Data were also rejected for Earth elevation angles (ELV) less than $5^\circ$, Earth day-time elevation angles (DYE_ELV) less than $20^\circ$, and values of the magnetic cut-off rigidity (COR) less than 6 GeV/$c^2$. Residual uncertainties in the XIS energy scale are of the order of 0.2 per cent or less (or $\sim 13$ eV at 6.4 keV – see Koyama et al. 2007). The cleaning and data selection resulted in net exposure times that are reported in Table 1.

The XIS2 detector was not operational by the time of the Fairall 9 observation so only data from XIS0, XIS1, and XIS3 were available for analysis. We extracted XIS spectra of Fairall 9 by using a circular extraction region with a radius of 3.5'. Background XIS spectra were made from off-source areas of the detector, after removing a circular region with a radius of 4.5' centered on the source, and the calibration sources (using rectangular masks). The background subtraction method for the HXD/PIN used the file `ae702043010_hxd_pinbgd.evt`, corresponding to the "tuned" version of the background model[2].

Spectral response matrix ("RMF") files, and telescope effective area ("ARF") files for the XIS data were made using the *Suzaku* FTOOLS XISRMFGEN and XISSIMARFGEN respectively. The XIS spectra from XIS0, XIS1, and XIS3 were combined into a single spectrum for spectral fitting. The three "RMF" and three "ARF" files were all combined, using the appropriate weighting (according to the count rates and exposure times for each XIS), into a single response file for the combined XIS background-subtracted spectrum of Fairall 9. For the HXD/PIN spectrum, the supplied spectral response matrix appropriate for the time of the observation (`ae_hxd_pinxinome3_20080129.rsp`) was used for spectral fitting.

The useful energy bandpass for the spectrum from each instrument was determined by the systematics of the background subtraction. For the XIS, a useful bandpass of 0.50–9.1 keV was determined, for which the background was less than 20 per cent of the source counts in any spectral bin. The width of the bins for the XIS data was 30 eV. With this spectral binning, all bins in the 0.50–9.10 keV range had greater than 20 counts, enabling the use of the $\chi^2$ statistic for spectral fitting. (We avoid grouping spectral bins using a signal-to-noise ratio threshold because it can "wash out" absorption features.) In addition to omitting data on the basis of background-subtraction systematics, we also omitted some spectral data that are subject to

[1] http://heasarc.gsfc.nasa.gov/docs/suzaku/analysis/pinbgd.html
[2] See http://heasarc.gsfc.nasa.gov/docs/suzaku/analysis/pinbgd.html

**Table 1.** Exposure times and count rates for the *Suzaku* spectra

| Detector | Exposure (ks) | Energy Range (keV) | Rate[a] (count $s^{-1}$) | Percentage of on-source rate[b] |
|---|---|---|---|---|
| XIS | 167.8 | 0.5–1.7, 1.9–2.1, 2.35–9.1 | $0.7535 \pm 0.0013$ | 98.3 per cent |
| PIN | 127.3 | 12.5–42.5 | $0.0862 \pm 0.0021$ | 16.4 per cent |

[a] Background-subtracted count rate in the energy bands specified. For the XIS, this is the rate per XIS unit, averaged over XIS0, XIS1, and XIS3. [b] The background-subtracted source count rate as a percentage of the total on-source count rate, in the energy intervals shown.

calibration uncertainties in the effective area due to certain atomic features. It is known that the effective area calibration is poor in the ranges $\sim$ 1.8–1.9 keV (due to Si in the detector) and $\sim$ 2.0–2.4 keV (Au M edges due to the telescope). The effective area also has a significant, steep change at $\sim$ 1.56 keV (due to Al in the telescope). We took the conservative approach of omitting XIS data in the 1.7–1.9 and 2.1–2.35 keV energy ranges for the purpose of spectral fitting. For the HXD/PIN, spectral bins with negative background-subtracted counts clearly indicate a breakdown of the background model in those bins. We found that the spectral data in the energy range 12.5–42.5 keV produced greater than 20 counts per bin (after background subtraction), for bin widths of 3 keV. This gives the most reliable HXD/PIN spectrum with minimal binning whilst at the same time qualifying the spectrum for spectral fitting using the $\chi^2$ statistic. The selected energy ranges for the XIS and HXD/PIN are summarized in Table 1, along with the corresponding count rates.

The calibration of the relative cross-normalizations of the XIS and PIN data involves many factors (e.g. see Yaqoob (2012) for a detailed discussion). For observations that had the "XIS-nominal" pointing, such as the present *Suzaku* observation of Fairall 9, the PIN:XIS ratio (hereafter $C_{\rm PIN:XIS}$), recommended by the *Suzaku* Guest Observer Facility (GOF) is 1.16[3]. However, this value does not take into account background-subtraction systematics, sensitivity to the spectral shape, and other factors that could affect the actual ratio. On the other hand, allowing $C_{\rm PIN:XIS}$ to be a free parameter could potentially skew the best-fitting parameters of a model at the expense of settling on a value of $C_{\rm PIN:XIS}$ that is unrelated to the actual normalization ratio of the two instruments. Consequently, we performed spectral fits for both cases ($C_{\rm PIN:XIS}$ free, and $C_{\rm PIN:XIS}$ fixed at 1.16). In addition, a spectral fit was performed using only the XIS data.

We note that Fairall 9 was observed by *Suzaku* again on 2010 May 19, for $\sim$ 220 ks. However, this observation suffered from severe attitude problems, which have been described in detail in Lohfink et al. (2012a). The analysis of these data is complicated because the effective area and spectral response function calculations are compromised. Although Lohfink et al. (2012a) proceeded to analyse the data by creating a new attitude solution (as described in Nowak et al. 2011), the software tool that generates the effective area for spectral response functions, XISSIMARFGEN, was not designed to handle such large excursions in attitude (see Ishisaki et al. 2007 for a detailed description of XISSIMARFGEN). The resulting errors in the effective area are unquantified. In fact Lohfink et al. (2012a) pointed out that the XIS effective area and spectral response function below $\sim$ 2 and above $\sim$ 8 keV were clearly erroneous. However, the errors in the effective area in the rest of the data remain unquantified. We therefore did not analyse the 2010 *Suzaku* data because the results would be unreliable.

## 3 MODELING THE Fe K$\alpha$ LINE AND REFLECTION CONTINUUM

In Fig. 1(a) we show the unfolded *Suzaku* XIS and PIN spectra of Fairall 9 compared to a simple power-law continuum with an arbitrary normalization, and photon index, $\Gamma$, of 1.8 (a value typical of the intrinsic continuum of Seyfert galaxies in the pertinent energy range). The actual values of the normalization and $\Gamma$ are not important here because the purpose of the plot is simply to show the salient characteristics of the overall spectrum. Full spectral-fitting will then yield the actual parameters of the intrinsic continuum. Fig. 1(b) shows the data/model ratio. It can be seen from Fig. 1 that above $\sim$ 3 keV the spectrum shows the classic form of an Fe K$\alpha$ emission line peaking in the $\sim$ 6–7 keV rest-frame energy range, with a "tail" on the red side of the peak, and a broad, high-energy continuum "bump" above $\sim$ 10 keV. In Fairall 9 and many other AGN, it is these features that have been interpreted in terms of Fe fluorescence and Compton scattering in the strong gravity regime in the inner accretion disc within a few gravitational radii of a spinning black hole (e.g. Walton et al. 2013, and references therein). Fig. 1 also shows that the spectrum below $\sim$ 3 keV steepens considerably towards low energies, resulting in a "soft excess."

In addition to applying the so-called "blurred reflection" model to account for the apparent relativistically smeared accretion-disc X-ray spectral signatures in the Fairall 9 *Suzaku* data, Walton et al. (2013) also included an ad hoc Gaussian component and an additional disc-reflection continuum to model the narrow Fe K$\alpha$ line from distant matter (at tens of

[3] ftp://legacy.gsfc.nasa.gov/suzaku/doc/xrt/suzakumemo-2008-06.pdf

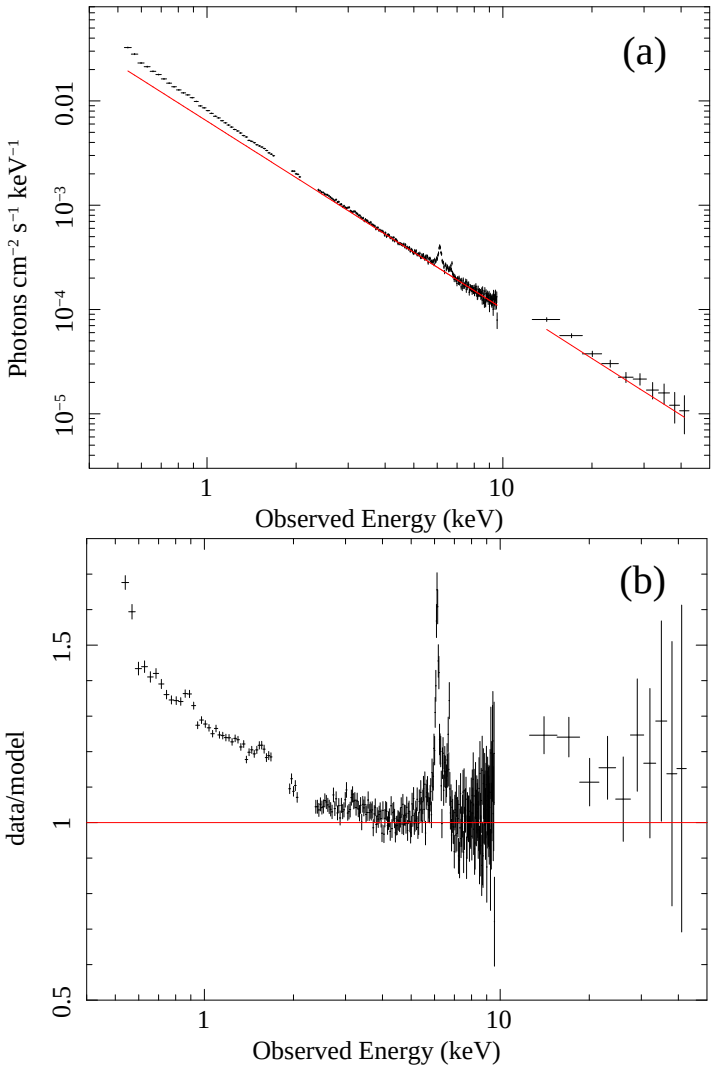



**Figure 1.** (a) The unfolded *Suzaku* XIS and PIN spectra of Fairall 9, compared to a power-law with a photon index of 1.8. The data below and above 10 keV are from the XIS and PIN respectively, and the data from XIS0, XIS1, and XIS3 are combined. Note that the PIN:XIS normalization ratio adopted for the plot was 1.16. (b) The data/model ratio corresponding to (a), in which the Fe K$\alpha$ line and high-energy "hump" are prominent features, which we show in §4 can be explained completely by nonrelativistic physics in distant matter, thousands of gravitational radii from the central black hole.

thousands of gravitational radii from the putative central black hole). The primary goal of the present spectral-fitting analysis is to determine whether the Fe K$\alpha$ emission line and X-ray reflection continuum in the *Suzaku* X-ray spectrum of Fairall 9 can be modeled *only* with a narrow Fe K$\alpha$ emission line and X-ray reflection continuum from distant matter with a finite column density, with the line and reflection continuum calculated self-consistently. Since we will use a model of the X-ray reprocessor that has a finite column density, we will be able to derive constraints on the global column density of the matter that produces the Fe K$\alpha$ emission line and X-ray reflection continuum. Fig. 1 shows that since the X-ray spectrum of Fairall 9 is rising continuously towards lower energies, the material that produces the Fe K$\alpha$ line cannot be obscuring the line-of-sight. A toroidal geometry for the X-ray reprocessor, observed at an inclination angle that does not intercept the line-of-sight, is therefore consistent with this scenario. (A disc geometry is also compatible, and has already been applied by Walton et al. 2013, but there is no such model with a finite column density, suitable for spectral fitting, that is publicly available.) We will apply the toroidal X-ray reprocessor model, MYTORUS (as described in Murphy & Yaqoob 2009, and Yaqoob 2012). An alternative spectral-fitting model with a different toroidal geometry to that of the MYTORUS model, due to Brightman & Nandra (2011), is also available. However, a detailed study by Liu & Li (2015) has shown that their model suffers from some erroneous calculations of the reprocessed X-ray continuum and line spectra, so we did not apply this model. We also note that the toroidal model of Ikeda et al. (2009) is not publicly available, and the CTORUS model (Liu & Li 2014) only became publicly available after the present study on Fairall 9 was completed.

Preliminary spectral fitting showed that a second power-law continuum component, in addition to a principal intrinsic

power-law component for the main hard continuum, was sufficient to account for the steep soft X-ray continuum . In general, there is a variety in the complexity of the soft excess in AGN, and there is still much debate as to its origin (e.g. see Middleton, Done & Gierliński 2007, Sobolewska & Done 2007). Although the soft part of the model ionised disc-reflection spectrum of the blurred reflection model can sometimes account for the soft excess, there are cases when it cannot. In particular, Lohfink et al. (2012a) found that a continuum component in addition to the blurred reflection spectrum had to be introduced to account for the soft excess in one of the *Suzaku* observations of Fairall 9. The blurred reflection model is certainly not a unique interpretation of the soft excess. For our purpose, the particular parameterization of the soft X-ray continuum does not affect our model of the narrow Fe K$\alpha$ line from neutral matter, and its associated reflection continuum. Therefore, we used a dual power law for the intrinsic continuum, with the photon indices and normalizations allowed to be free parameters. We refer to the photon indices of the hard and soft continua as $\Gamma_h$ and $\Gamma_s$ respectively. For the magnitude of the soft component, the actual fitting parameter was the ratio of the normalization of the soft component to the hard component at 1 keV, instead of the absolute normalization of the soft component. This ratio is denoted by $r_{\rm PL}$.

In addition to the irrelevance of the details of the soft excess model to our self-consistent modeling of the Fe K$\alpha$ line and Compton-reflection continuum, we found that below 1.5 keV the spectra from the three XIS detectors showed discrepancies with respect to each other that are larger than the statistical errors. These systematics are as large as 10 per cent above 0.7 keV, and $\sim 30$ per cent below 0.7 keV. The systematic differences in the spectra are likely dominated by the limitations in the calibration of the effect of contaminants on the CCDs, which have a spatial and temporal dependence. Above 1.5 keV the spectra from all three XIS detectors are statistically consistent with each other. Given these considerations, we performed all spectral fitting (using the combined XIS spectra) above 1.5 keV. The energy ranges above 1.5 keV used in the fits were as shown in Table 1.

We did not apply a high-energy cut-off in the form of an exponential diminishing factor that is often used, because such a form is unphysical. The X-ray reprocessor model that we use instead has a termination energy for the incident continuum, and different model tables are available for different termination energies (see Murphy & Yaqoob 2009). This is a closer approximation to actual X-ray spectra formed by Comptonisation in a single-temperature plasma, which are characterized by a power law form up to some energy, followed by a rollover, as opposed to the continuous change in slope of exponential cut-off models. However, the more physically motivated models are not necessarily statistically superior to the empirical models in the sense that the two types of model cannot always be distinguished by the data. For example, in a study of 202 X-ray observations of Cyg X-1, Wilms et al. (2006) found that only 12 observations were better described by a Comptonisation model as opposed to an empirical model with an exponential cut-off. In the case of Fairall 9, the *Suzaku* HXD/PIN spectrum for Fairall 9 only has useful data extending to $\sim 43$ keV (see Fig. 1), so steepening of the high-energy continuum is not easily discernible, especially given the fact that the X-ray reprocessor models themselves cause their own high-energy steepening of the observed spectra, due to Compton downscattering in the circumnuclear matter. With *BeppoSAX*, the spectrum of Fairall 9 was measured out to $\sim 100$ keV but the statistical quality of the data was insufficient to determine if the spectrum begins to cut off below 100 keV (Dadina 2007). More recently, multi-epoch fitting of *XMM-Newton* and *NuSTAR* spectra with an exponential cut-off yielded only a lower limit on the cut-off energy of 933 keV (Lohfink et al. 2016), although the actual value is model-dependent. Therefore, in our modeling of the *Suzaku* data, the use of a Comptonisation model for the intrinsic continuum is not necessary. However, it is important to note that whatever the form of the intrinsic continuum, in the model, that continuum must extend to higher energies than the highest energy of the data. This is because high-energy photons can be downscattered (many times if the medium is Compton-thick) to within the range of the data bandpass, contributing to the observed continuum, as well as to fluorescent line emission.

We used XSPEC (Arnaud 1996) [4] for spectral fitting and utilized the $\chi^2$ statistic for minimization. In all of the model fits we included Galactic absorption with a column density of $3.18 \times 10^{20}$ cm$^{-2}$, obtained with the FTOOL nh, based on the LAB survey described in Kalberla et al. (2005). We used photoelectric cross sections given by Verner et al. (1996). Solar element abundances from Anders & Grevesse (1989) were used throughout. All astrophysical model parameter values will be given in the rest frame of Fairall 9 unless otherwise stated. For the sake of brevity, certain quantities and details pertaining to particular spectral fits will be given in the tables of results and not repeated again in the text, unless it is necessary. Specifically, we are referring to the number of free parameters in a fit, the number of degrees of freedom, and the null hypothesis probability. Statistical errors given will be given for one-parameter, 90 per cent confidence (corresponding to a $\Delta\chi^2$ criterion of 2.706).

In a given energy band in the observed frame, observed fluxes will be denoted by $F_{\rm obs}$, and observed luminosities will be denoted by $L_{\rm obs}$. These quantities are not corrected for absorption nor Compton scattering in either the line-of-sight material, or in the circumnuclear material. On the other hand, intrinsic luminosities, denoted by $L_{\rm intr}$ will be corrected for absorption and X-ray reprocessing. The energy band associated with a particular value of $L_{\rm obs}$ or $L_{\rm intr}$ will refer to the energy range in the rest frame of the source. We use a standard cosmology of $H_0 = 70$ km s$^{-1}$ Mpc$^{-1}$, $\Lambda = 0.73$, $q_0 = 0$ throughout the paper.

[4] http://heasarc.gsfc.nasa.gov/docs/xanadu/xspec/

### 3.1 The MYTORUS Model

The toroidal X-ray reprocessor model, MYTORUS, has been described in detail in Murphy & Yaqoob (2009) and Yaqoob & Murphy (2011). The baseline geometry consists of a torus with a circular cross section, whose diameter is characterized by the equatorial column density, $N_{\rm H}$. The torus is composed of neutral matter and is illuminated by a central, isotropic X-ray source, and the global covering factor of the reprocessor is 0.5, corresponding to a solid angle subtended by the structure at the central X-ray source of $2\pi$ (which in turn corresponds to an opening half-angle of $60^\circ$). The MYTORUS model self-consistently calculates the Fe K$\alpha$ and Fe K$\beta$ fluorescent emission-line spectrum and the effects of absorption and Compton scattering on the X-ray continuum and line emission. The element abundances in the MYTORUS model are those of the solar values of Anders & Grevesse (1989), and the photoelectric absorption cross-sections are those of Verner et al. (1996). However, currently, none of the element abundances can be varied in the MYTORUS model. The practical implementation of the MYTORUS model allows free relative normalizations between different components of the model in order to accommodate for differences in the actual geometry pertinent to the source (compared to the specific model assumptions used in the original calculations), and for time delays between direct continuum, Compton-scattered continuum, and fluorescent line photons[5]. However, self-consistency between the fluorescent line emission and the reflection continuum is always maintained.

The so-called zeroth-order continuum component of the model is the direct, line-of-sight observed continuum. If the orientation of the toroidal symmetry axis is such that the angle between that axis and the line-of-sight to the observer (hereafter $\theta_{\rm obs}$) is greater than the opening half-angle, the zeroth-order continuum is diminished by absorption and Compton-scattering into directions away from the line-of-sight. The zeroth-order continuum is thus obtained from the intrinsic continuum by application of a multiplicative table model and is not affected by the global geometry of the model. On the other hand, the global Compton-scattered continuum (or reflection spectrum) is implemented as an XSPEC additive table model. We used the table `mytorus_scatteredH200_v00.fits`, which corresponds to a power-law incident continuum with a termination energy of 200 keV, and a photon index ($\Gamma$) in the range 1.4–2.6. The Fe K$\alpha$ and Fe K$\beta$ emission lines are implemented with another (single) XSPEC additive table model that is produced from the same self-consistent Monte Carlo calculations that were used to calculate the corresponding Compton-scattered continuum table (we used the table `mytl_V000010nEp000H200_v00.fits`). The parameters for each of the three additive tables are the normalization of the incident power-law continuum ($A_{\rm PL}$), $\Gamma$, $\theta_{\rm obs}$, and redshift ($z$).

We denote the relative normalization between the scattered continuum and the direct, intrinsic continuum, by $A_S$, which has a value of 1.0 for the assumed geometry. This value also implies that either the intrinsic X-ray continuum flux is constant, or, for a variable intrinsic X-ray continuum, that the X-ray reprocessor is compact enough for the Compton-scattered flux to respond to the intrinsic continuum on timescales much less than the integration time for the spectrum. Conversely, departures from $A_S = 1.0$ imply departure of the covering factor from 0.5, or time delays between the intrinsic and Compton-scattered continua, or both. However, it is important to note that $A_S$ is *not* simply related to the covering factor of the X-ray reprocessor because the detailed shape of the Compton-scattered continuum varies with covering factor. Analogously to $A_S$, the parameter $A_L$ is the relative normalization of the Fe K$\alpha$ line emission, with a value of 1.0 having a similar meaning to that for $A_S = 1.0$. In our analysis we will set $A_L = A_S$ (relaxing this assumption would imply significant departure from the default model, such as non-solar Fe abundance). In practice, $A_S$ and $A_L$ are each implemented in XSPEC by a "constant" model component that multiplies the Compton-scattered continuum and fluorescent line table respectively, which for $A_L = A_S$ are tied together. All of the remaining parameter values in the various MYTORUS tables (described above) are required to be tied together by definition of the model tables. The MYTORUS model can be applied in a number of ways that have been detailed in Yaqoob (2012), LaMassa et al. (2014), and Yaqoob et al. (2015), but the application to Fairall 9 and other unobscured AGN is particularly simple because only lines of sight that do not intercept the torus are relevant. Therefore, we do not need to include the zeroth-order continuum component.

### 3.2 The Fe K$\alpha$ Line Energy

In the MYTORUS model the centroid energies of the Fe K$\alpha$ and Fe K$\beta$ lines emission are not free parameters since the lines are explicitly modeled as originating in neutral matter. In fact, in the MYTORUS model, the Fe K$\alpha$ line is explicitly modeled as the doublet K$\alpha_1$ at 6.404 keV and K$\alpha_2$ at 6.391 keV, with a branching ratio of 2:1, which results in a weighted mean centroid energy of 6.400 keV (see Murphy & Yaqoob (2009) for details). The Fe K$\beta$ line is centered at 7.058 keV. For Fairall 9, Yaqoob & Padmanabhan (2004) empirically measured a peak rest-frame Fe K$\alpha$ line energy of $6.373^{+0.254}_{-0.092}$ keV using high-spectral-resolution *Chandra* HEG data and a simple Gaussian parameterization of the line shape (the Fe K$\beta$ line was not detected).

In practice, the peaks of the Fe K$\alpha$ and Fe K$\beta$ emission lines in the *Suzaku* data may be offset relative to the baseline model because of instrumental calibration systematics and/or mild ionisation. The *Suzaku* data are sensitive to offsets in the

[5] See http://mytorus.com/manual/ for details

Fe K$\alpha$ line peak as small as $\sim 10$ eV. Therefore, in the MYTORUS model we allowed the redshift parameter associated with the Fe K$\alpha$ and Fe K$\beta$ line table to vary independently of the redshift for all the other model components (which was fixed at the cosmological redshift of Fairall 9). After finding the best-fitting redshift for the line emission, the line redshift was frozen at that value before deriving statistical errors on the remaining free parameters of the model. In the tables of spectral-fitting results that we will present, the redshift offset will be given as the effective Fe K$\alpha$ line energy offset, $E_{\rm shift}$, in the observed frame (or $(1+z)E_{\rm shift}$ in the source frame, where $z$ is the cosmological redshift). A positive shift means that the Fe K$\alpha$ line centroid energy is higher than the expected 6.400 keV. In principle, an energy shift should also be applied to the reflection continuum, but this would require an additional parameter since the shift is not necessarily going to have the same value as that for the Fe K$\alpha$ line. However, since the reflection continuum is broad and the feature around the Fe K edge is weak compared to the total continuum, the shift would not impact the key model parameters and the additional shift parameter would be poorly constrained. Therefore a shift was not applied to the reflection continuum.

### 3.3 The Fe K$\alpha$ Line Velocity Width

In the application of the MYTORUS model, the velocity broadening of the Fe K$\alpha$ and Fe K$\beta$ lines is achieved with the `gsmooth` convolution model in XSPEC, which convolves the intrinsic line emission spectrum with a Gaussian that has a width $\sigma(E) = \sigma_0(E/6\ {\rm keV})^{\alpha}$, where $\sigma_0$ and $\alpha$ are the two parameters of the `gsmooth` model. Since the Doppler velocity width is $\Delta v \sim c(\sigma(E)/E)$, fixing $\alpha = 1$ models a velocity width that is independent of energy. The parameter $\sigma_0$ is then related to the FWHM by FWHM $\sim 2.354(c/6.0)\sigma_0 \sim 117,700\sigma_0$ km s$^{-1}$, if $\sigma_0$ is in keV. Both the Fe K$\alpha$ and Fe K$\beta$ lines are tied to a single width parameter, $\sigma_0$, since both lines originate in the same atoms. The spectral resolution of the *Suzaku* CCD detectors was of the order 7000 km s$^{-1}$ FWHM at the Fe K$\alpha$ line peak energy, at the time of the Fairall 9 observation. Since the width of the fluorescent emission lines provides an important constraint on the location of the X-ray reprocessor, we will also present, in §4.3, a re-analysis of the *Chandra* HEG (high-energy grating) data, which has a spectral resolution of $\sim 1860$ km s$^{-1}$ FWHM at 6.4 keV. The original analysis of the *Chandra* HEG data (Yaqoob & Padmanabhan 2004) simply utilized a Gaussian parameterization of the Fe K$\alpha$ line profile, whereas the presence of a Compton shoulder in the Fe K$\alpha$ line profile can affect the inferred velocity width (e.g. see Yaqoob & Murphy 2011). The relative magnitude of the Compton shoulder depends on the column density of the line-emitting matter, and we will use the MYTORUS fits to the *Suzaku* data to guide fitting the *Chandra* HEG data, since the *Chandra* data have a smaller bandpass and lower signal-to-noise ratio than the *Suzaku* data.

### 3.4 The Fe K$\alpha$ Line Flux and Equivalent Width

The Fe K$\alpha$ line flux is not explicitly an adjustable parameter because the line is produced self-consistently in the MYTORUS model of the X-ray reprocessor. However, by isolating the emission-line table of the MYTORUS model, keeping the best-fitting model parameters, we can measure the observed flux of the Fe K$\alpha$ line using an energy range that excludes the Fe K$\beta$ line. (The rest-frame flux is obtained by multiplying the observed flux by $(1+z)$.) The equivalent width (EW) of the Fe K$\alpha$ line was calculated using the line flux and the measured (total) monochromatic continuum model flux at the observed line peak energy. The EW in the source frame was then obtained by multiplying the observed EW by $(1+z)$. Note that the Fe K$\alpha$ line flux and EW include both the zeroth-order and the Compton shoulder components of the Fe K$\alpha$ line. Also, in the MYTORUS model, the Fe K$\beta$ line flux and EW are not independent of the Fe K$\alpha$ line parameters because the theoretical value of the Fe K$\beta$ to Fe K$\alpha$ branching ratio is already factored into the self-consistent Monte Carlo simulations on which the model is based (e.g. see Murphy & Yaqoob 2009).

Since the Fe K$\alpha$ line flux and EW are not explicit parameters, the statistical errors on them cannot be obtained in the usual way. However, in the MYTORUS fits, the fractional errors on the parameter $A_S$ are used as approximations for the fractional errors on the Fe K$\alpha$ line flux and EW.

## 4 SPECTRAL FITTING RESULTS

In this section we give the results of fitting the Fairall 9 *Suzaku* data with the MYTORUS model, with several variations in the choices of parameters that are not allowed to vary. In the *Suzaku* spectral fits it was also necessary to include two Gaussian components to model the narrow emission lines Fe XXV(r) and Fe XXVI Ly$\alpha$. These lines originate in an ionised region that must clearly be distinct from the matter distribution that produces the neutral Fe K$\alpha$ line and the associated reflection continuum. They were also included in previous analyses of the same *Suzaku* data for Fairall 9 (Schmoll et al. 2009; Patrick et al. 2011a; Lohfink et al. 2012a; Walton et al. 2013). The widths of both Gaussian components were fixed at 100 km s$^{-1}$ FWHM since the lines are unresolved. Each Gaussian component then has two free parameters, namely the centroid energy, and the line flux. On the other hand, the width of the Fe K$\alpha$ line was allowed to float, and we also give the

**Table 2.** Spectral-fitting results

| Parameter | | | | | |
|---|---|---|---|---|---|
| Mission | *Suzaku* | *Suzaku* | *Suzaku* | *Suzaku* | *Chandra* |
| Instruments | PIN,XIS | PIN,XIS | PIN,XIS | XIS | HEG |
| Free Parameters | 13 | 12 | 13 | 12 | 6 |
| $\chi^2$ / degrees of freedom | 248.7/238 | 254.1/239 | 247.4/238 | 244.3/239 | ... |
| Reduced $\chi^2$ | 1.045 | 1.063 | 1.039 | 1.067 | ... |
| Null Probability | 0.304 | 0.240 | 0.325 | 0.233 | ... |
| $C$ statistic | ... | ... | ... | ... | 900.6 |
| "Goodness" of fit | ... | ... | ... | ... | 36.9 per cent |
| $\theta_{\rm obs}$ (°) | 0 (f) | 0 (f) | 59 (f) | 0 (f) | 0 (f) |
| $C_{\rm PIN:XIS}$ | $1.32^{+0.11}_{-0.11}$ | 1.16 (f) | $1.30^{+0.12}_{-0.11}$ | ... | ... |
| $N_{\rm H}$ ($10^{24}$ cm$^{-2}$) | $0.902^{+0.206}_{-0.216}$ | $1.603^{+0.366}_{-0.312}$ | $0.795^{+0.169}_{-0.169}$ | $1.000^{+3.000}_{-0.371}$ | 0.902 (f) |
| $A_S$ | $1.370^{+0.099}_{-0.086}$ | $1.491^{+0.122}_{-0.122}$ | $1.763^{+0.112}_{-0.124}$ | $1.364^{+0.635}_{-0.104}$ | $1.60^{+2.29}_{-1.15}$ |
| $\Gamma_h$ | $1.904^{+0.016}_{-0.017}$ | $1.895^{+0.016}_{-0.020}$ | $1.920^{+0.014}_{-0.018}$ | $1.920^{+0.018}_{-0.024}$ | 1.904 (f) |
| $\Gamma_s$ | $7.10^{+1.67}_{-1.32}$ | $6.88^{+1.54}_{-1.25}$ | $7.60^{+1.73}_{-1.24}$ | $7.10^{+0.16}_{-0.14}$ | 7.10 (f) |
| $r_{\rm PL}$ | $1.63^{+1.74}_{-0.68}$ | $1.56^{+1.46}_{-0.62}$ | $1.88^{+2.19}_{-0.87}$ | $1.66^{+0.12}_{-0.12}$ | 1.63 (f) |
| $E_{\rm shift}$ (eV) | $20.0^{+7.9}_{-6.0}$ | $22.2^{+6.5}_{-5.8}$ | $19.7^{+8.1}_{-5.9}$ | $22.2^{+5.8}_{-8.1}$ | $22.5^{+19.6}_{-16.2}$ |
| $I_{\rm Fe\ K\alpha}$ ($10^{-5}$ photons cm$^{-2}$ s$^{-1}$) | $3.14^{+0.23}_{-0.20}$ | $3.17^{+0.26}_{-0.26}$ | $2.96^{+0.19}_{-0.21}$ | $3.14^{+1.46}_{-0.24}$ | $3.26^{+1.43}_{-0.92}$ |
| EW$_{\rm Fe\ K\alpha}$ (eV) | $123^{+9}_{-8}$ | $124^{+10}_{-10}$ | $121^{+8}_{-9}$ | $123^{+57}_{-10}$ | $143^{+63}_{-40}$ |
| FWHM[Fe K$\alpha$, Fe K$\beta$ ] (km s$^{-1}$) | $4475^{+1730}_{-2065}$ | $4355^{+1810}_{-2105}$ | $4285^{+1650}_{-2390}$ | $4355^{+1805}_{-2005}$ | $3390^{+11350}_{-1040}$ |
| $E_{\rm Fe\ XXV}$ (keV) | $6.752^{+0.038}_{-0.038}$ | $6.744^{+0.048}_{-0.031}$ | $6.751^{+0.042}_{-0.039}$ | $6.752^{+0.037}_{-0.039}$ | 6.752 (f) |
| $I_{\rm Fe\ XXV}$ ($10^{-5}$ photons cm$^{-2}$ s$^{-1}$) | $0.43^{+0.15}_{-0.15}$ | $0.42^{+0.15}_{-0.15}$ | $0.40^{+0.15}_{-0.16}$ | $0.43^{+0.15}_{-0.15}$ | $< 0.82$ |
| EW$_{\rm Fe\ XXV}$ (eV) | $16.8^{+5.9}_{-5.9}$ | $17.7^{+6.4}_{-6.5}$ | $16.9^{+6.3}_{-6.8}$ | $18.2^{+6.4}_{-6.4}$ | $< 39$ |
| FWHM[Fe XXV] (km s$^{-1}$) | 100 (f) | 100 (f) | 100 (f) | 100 (f) | 100 (f) |
| $E_{\rm Fe\ XXVI}$ (keV) | $6.970^{+0.039}_{-0.032}$ | $6.975^{+0.033}_{-0.044}$ | $6.975^{+0.035}_{-0.040}$ | $6.975^{+0.034}_{-0.037}$ | 6.970 (f) |
| $I_{\rm Fe\ XXVI}$ ($10^{-5}$ photons cm$^{-2}$ s$^{-1}$) | $0.41^{+0.16}_{-0.16}$ | $0.39^{+0.16}_{-0.16}$ | $0.38^{+0.16}_{-0.16}$ | $0.40^{+0.15}_{-0.15}$ | $< 1.15$ |
| EW$_{\rm Fe\ XXVI}$ (eV) | $18.5^{+7.2}_{-7.2}$ | $17.5^{+7.1}_{-7.0}$ | $19.7^{+8.1}_{-5.9}$ | $18.2^{+6.8}_{-6.8}$ | $< 58$ |
| FWHM[Fe XXVI] (km s$^{-1}$) | 100 (f) | 100 (f) | 100 (f) | 100 (f) | 100 (f) |
| $F_{\rm obs}$[2–10 keV] ($10^{-11}$ erg cm$^{-2}$ s$^{-1}$) | 2.31 | 2.32 | 2.35 | 2.35 | 2.11 |
| $F_{\rm obs}$[10–30 keV] ($10^{-11}$ erg cm$^{-2}$ s$^{-1}$) | 2.09 | 2.33 | 2.12 | ... | ... |
| $L_{\rm obs}$[2–10 keV] ($10^{44}$ erg s$^{-1}$) | 1.20 | 1.20 | 1.22 | 1.22 | 1.09 |
| $L_{\rm obs}$[10–30 keV] ($10^{44}$ erg s$^{-1}$) | 1.08 | 1.20 | 1.10 | ... | ... |
| $L_{\rm intr}$[2–10 keV] ($10^{44}$ erg s$^{-1}$) | 1.22 | 1.19 | 1.15 | 1.15 | 1.02 |
| $L_{\rm intr}$[10–30 keV] ($10^{44}$ erg s$^{-1}$) | 0.89 | 0.90 | 0.87 | ... | ... |

Spectral-fitting results for *Suzaku* and *Chandra* HEG data for Fairall 9, obtained from fitting with the MYTORUS model. Fixed parameters are indicated by (f). The best-fitting energy shifts of the Fe K$\alpha$ line model, $E_{\rm shift}$, are given at the line peak in the observed frame. All remaining parameters are given in the AGN frame. In order to obtain the statistical errors on the parameters, in some cases, one or more of the other parameters had to be temporarily frozen to avoid the spectral fit becoming unstable. See text for details on this and other aspects of the spectral fitting.

results of a re-analysis of a *Chandra* high-energy grating observation of Fairall 9 in order to supplement the *Suzaku* constraints on the Fe K$\alpha$ line width. For the sake of reproducibility, we give the complete XSPEC model expression:

$$\begin{aligned}\text{MYTORUS model} = {} & \text{constant} < 1 > * \text{phabs} < 2 > ( \\ & \text{constant} < 3 > * \text{zpowerlw} < 4 > + \text{zpowerlw} < 5 > \quad + \\ & \text{constant} < 6 > * \text{atable}\{\text{mytorus\_scatteredH200\_v00.fits}\} < 7 > \quad + \\ & \text{constant} < 8 > * (\text{gsmooth} < 9 > (\text{atable}\{\text{mytl\_V000010nEp000H200\_v00.fits}\} < 10 >)) \quad + \\ & \text{zgauss} < 11 > + \text{zgauss} < 12 > )\end{aligned}$$

The model parameters have been described in §3.1. Here we identify constant $< 1 >$= C$_{\rm PIN:XIS}$, phabs $< 2 >$= Galactic column density, constant $< 6 > = A_S$, and constant $< 8 > = A_L$. According to the way that the MYTORUS model tables are constructed, the column densities associated with each of the two tables (components 7 and 10 above) must be tied together, as is also the case for the inclination angles. The two intrinsic power-law continuum components are represented by zpowerlw $< 4 >$ and zpowerlw $< 5 >$, associated with photon indices $\Gamma_s$ and $\Gamma_h$ respectively. The MYTORUS model is linked to only one of these intrinsic continuum components (the harder power law, with photon index $\Gamma_h$). The component that

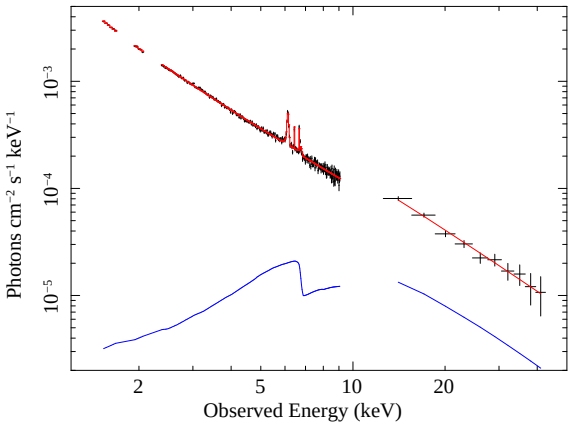



**Figure 2.** Broadband spectral fit to the *Suzaku* Fairall 9 data with the best-fitting face-on MYTORUS model with $C_{\rm PIN:XIS}$ free (see §4 and Table 2, column 2). Shown are the unfolded spectral data (black), the net model spectrum overlaid on the data (red), and the Compton-scattered (reflection) continuum contribution (lower, blue curve) that is included in the net model spectrum. Note that in unfolded spectra, some emission-line features appear to be artificially narrower than they really are. See Fig. 3, which shows the same fit as shown here, but with the model overlaid on the counts spectrum, which does not suffer from this effect. (A color version of this figure is available in the online journal.)

models the soft X-ray continuum is too steep to produce any significant Fe K$\alpha$ line emission and X-reflection continuum, in comparison to the fluorescence and reflection features due to the flatter, hard X-ray continuum. The ratio of normalizations of the soft and hard power-law continua (i.e. the ratio of fluxes at 1 keV), is denoted by the parameter $r_{\rm PL}$ (constant $< 3 >$ in the above model expression).

For lines of sight to the observer that do not intersect the torus (i.e. for $\theta_{\rm obs} < 60^\circ$), the shape of the X-ray reflection continuum and the EW of the Fe K$\alpha$ line are not very sensitive to the actual inclination angle. For our baseline spectral-fitting model, we fixed the inclination angle of the torus, $\theta_{\rm obs}$, at 0°, and allowed $C_{\rm PIN:XIS}$, the *Suzaku* PIN:XIS normalization ratio, to be free. The model gives an excellent fit to the data, with a reduced $\chi^2$ of 1.045, and the results are shown in column 2 of Table 2.

This baseline model fit is shown overlaid on the unfolded *Suzaku* spectrum in Fig. 2, with the contribution from the reflection continuum also shown separately in order to demonstrate its magnitude relative to the total continuum. Fig. 3(a) further illustrates the spectral fit, showing the model overlaid on the counts spectrum, whilst Fig. 3(b) shows the data/model ratio. Fig. 3(c) shows a zoom on the Fe K band of the model overlaid on the counts spectrum, and Fig. 3(d) shows the corresponding data/model ratio. The data/model ratios show the quality of the fit, and in particular, the remarkably flat residuals in Fig. 3(d) show that the model fits the Fe K$\alpha$ line, the Fe K$\beta$ line, and the Fe K edge extremely well. This is despite the fact that no ad hoc or empirical adjustments were applied to either of the Fe fluorescent lines relative to the Compton-scattered continuum, and the Fe abundance was fixed at the solar value. For a given set of model parameters that determine the Compton-scattered continuum, the Fe fluorescent lines are completely determined. This self-consistent solution also shows flat residuals on the red side of the Fe K$\alpha$ line peak, implying that no additional complexity in the model is required. In other words, a relativistically broadened Fe K$\alpha$ line is not required, and the narrow Fe K$\alpha$ line alone is sufficient to account for the data. Since the data/model ratio in Fig. 3(c) is statistically consistent with 1.0, it is clear that any additional model complexity would simply be fitting the noise. Nevertheless, in §4.7 we will obtain upper limits on the magnitude of a contribution from possible relativistically blurred reflection and Fe K$\alpha$ line emission, as well as illustrating how the MYTORUS model is able to reduce the required magnitude of such spectral components.

The best-fitting value of $C_{\rm PIN:XIS}$ for the baseline model is $1.32 \pm 0.11$ (Table 2, column 2), which is rather high compared to the "official" recommended value of 1.16 for XIS-nominal *Suzaku* observations. The high value could be due to background-subtraction systematic uncertainties of the PIN data, and this effect for the baseline model will be quantified in §4.6. In order to explore the robustness of the baseline model, Table 2 also shows the results of three variations on the baseline model fit. In the first of these (column 3 in Table 2), the PIN:XIS normalization ratio, $C_{\rm PIN:XIS}$, is fixed at the value of 1.16. The data/model ratios for this fit are shown in Fig. 3(e) and Fig. 3(f), and they can be directly compared with the corresponding ratios for the fit with $C_{\rm PIN:XIS}$ free in Fig. 3(c) and Fig. 3(d) respectively. It can be seen that the main difference in the data/model ratios for the two fits is that in the fit with $C_{\rm PIN:XIS}$ fixed there is an excess in the PIN data below $\sim 20$ keV. On the other hand, in the Fe K band the differences in the data/model ratios are insignificant (compare Fig. 3(d) and Fig. 3(f)). Next, in a third spectral fit, $C_{\rm PIN:XIS}$ is again allowed to be free, but the inclination angle of the torus is fixed at $\theta_{\rm obs} = 59^\circ$ (i.e., just below the value of 60° that would make the line of sight graze the surface of the torus). The results for this case are shown in column 4 of Table 2 and can be used to assess the impact of the different inclination angles on the other model

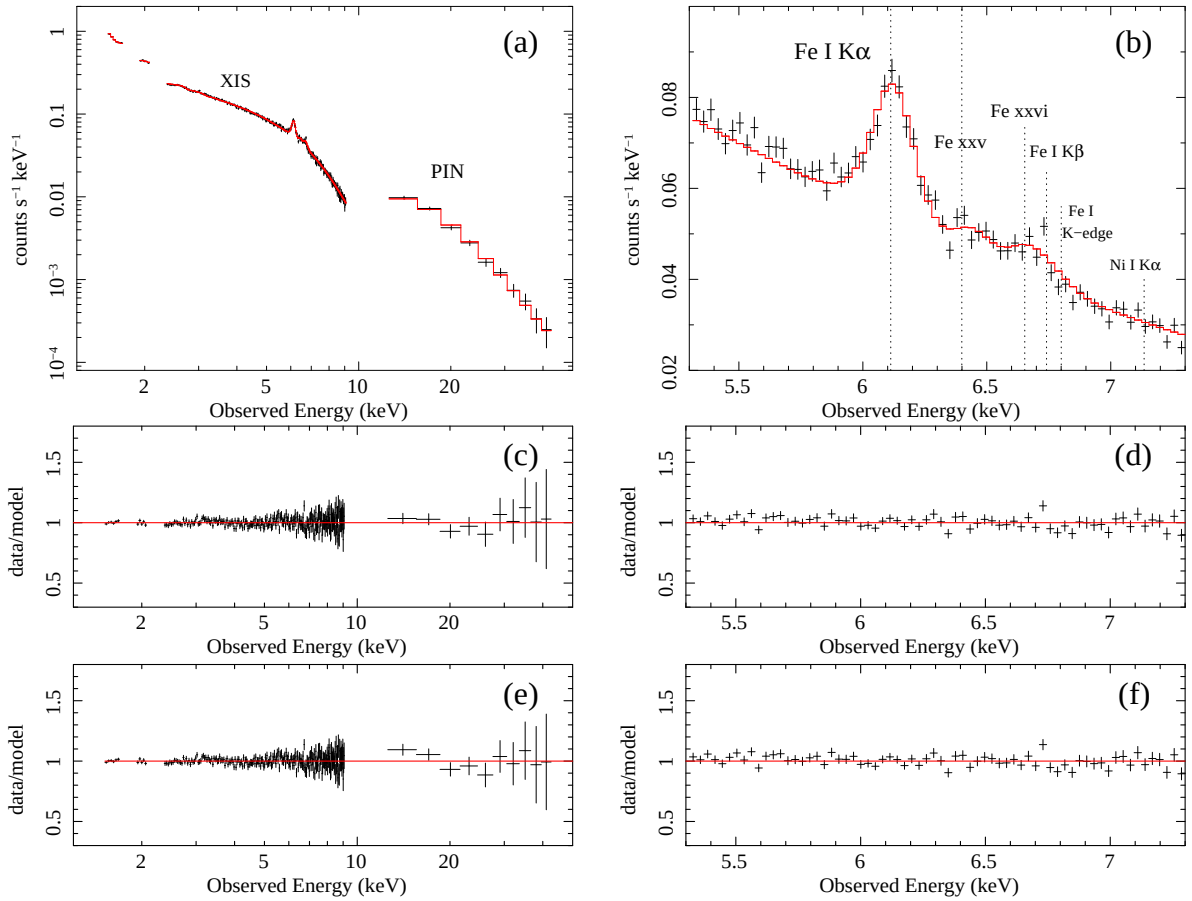



**Figure 3.** (a) The same broadband spectral fit as in Fig. 2 (see §4 and Table 2, column 2), this time showing the best-fitting face-on MYTORUS model with $C_{\rm PIN:XIS}$ free (red) overlaid on the *Suzaku* counts spectra (black) for Fairall 9. Note that data in the energy ranges 1.7–1.9, and 2.1–2.35 keV are omitted due to calibration uncertainties (see text for details). (b) The data and model shown in (a), zoomed in on the Fe K region, showing the detailed fit to the Fe K$\alpha$ emission line and other atomic features as labeled. Note that the flux of the model Fe K$\alpha$ line is not controlled by an arbitrary parameter but calculated self-consistently from the same matter distribution that produces the global Compton-scattered continuum (see Fig. 2). The dotted lines correspond to the expected energies of the labeled atomic features in the observed frame. The data to model ratios corresponding to (a) and (b) are shown in (c) and (d) respectively. Panels (e) and (f) show the data to model ratios corresponding to the best-fitting face-on MYTORUS model with $C_{\rm PIN:XIS}$ fixed at the value of 1.16 (Table 2, column 3) for the broadband fit and Fe K region respectively. (A color version of this figure is available in the online journal.)

parameters. In the next fit (column 5 of Table 2), the inclination angle is reverted back to 0°, but this time only the XIS data are fitted. This fit completely eliminates any systematic uncertainty in the PIN:XIS normalization ratio, albeit at the expense of larger statistical errors on the fit parameters. All of these scenarios give excellent fits to the data, and details of the model parameters obtained from spectral fitting are discussed below, in §4.1 to §4.6. Note that in order to avoid the fits becoming unstable, some of the parameters had to be fixed in order to derive statistical errors for the remaining parameters. The parameters that had to be fixed under such circumstances were the Fe K$\alpha$ line shift, $E_{\rm shift}$, the Fe K$\alpha$ line width, and the centroid energies of the Fe XXV and Fe XXVI Ly$\alpha$ lines. In the fits in which $C_{\rm PIN:XIS}$ was a free parameter, statistical errors on $C_{\rm PIN:XIS}$ were obtained with the full set of free parameters as indicated in Table 2. Then statistical errors on $E_{\rm shift}$ were derived, after which $E_{\rm shift}$, $C_{\rm PIN:XIS}$, the Fe K$\alpha$ line width, and the centroid energies of the Fe XXV and Fe XXVI Ly$\alpha$ lines were frozen in order to derive statistical errors on the remaining parameters. The statistical errors on the Fe K$\alpha$ line width, and the centroid energies of the Fe XXV and Fe XXVI Ly$\alpha$ lines were derived by allowing each parameter to be free in turn.

The final column in Table 2 shows the results of fitting the MYTORUS model to *Chandra* high-energy grating (HEG) data from an observation of Fairall 9 made in 11 September, 2001. The same spectrum and energy band (2–7 keV) that were used in the original analysis of these data (as described in Yaqoob & Padmanabhan 2004) were used to fit the MYTORUS model. We applied the same baseline model that was applied to the *Suzaku* data (see column 2 of Table 2). However, due to the rather narrow bandpass of the HEG data used, we fixed many of the model parameters at the best-fitting *Suzaku* values from the baseline model. The results for the best-fitting parameters and their statistical uncertainties are shown in column 6 of Table 2. The spectrum and best-fitting model are shown in Fig. 4(a), and the residuals (difference between the data and

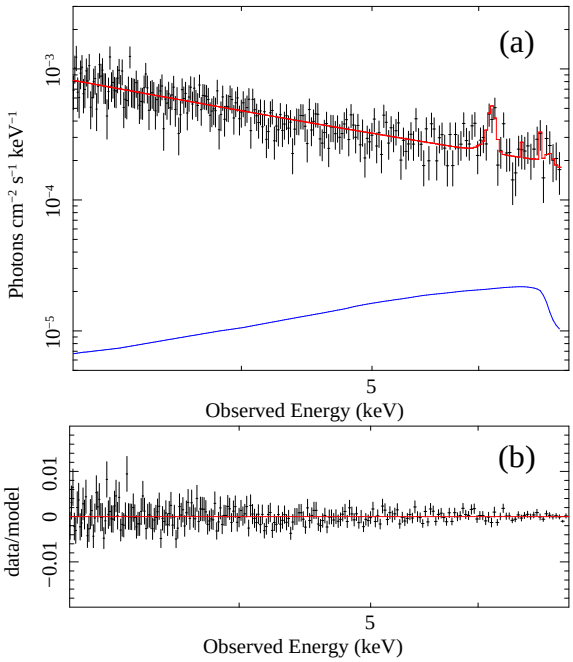



**Figure 4.** The baseline MYTORUS model fitted to the *Chandra* HEG spectrum (see §4 and Table 2, column 6), showing (a) the best-fitting model overlaid on the unfolded spectrum, and (b) the residuals (difference between data and model counts). (A color version of this figure is available in the online journal.)

model counts) are shown in Fig. 4(b). Also indicated in column 6 of Table 2 are the parameters that had to be fixed in the HEG fit. Only six parameters were free, namely the overall continuum normalization, $E_{\rm shift}$, $A_S$, $\sigma_0$ (Fe K$\alpha$ and Fe K$\beta$ line width), and the fluxes of the two narrow Fe XXV and Fe XXVI lines from ionised matter. Freezing the other parameters in the spectral fit does not compromise the principal objective of the MYTORUS fit, which is to attempt to take advantage of the superior spectral resolution of the *Chandra* HEG data, in order to supplement the *Suzaku* constraints on the velocity width of the Fe K$\alpha$ line. For the HEG spectral fit we used the $C$-statistic for minimization since the counts per channel in the spectrum are in the Poisson regime. We used the "goodness" command in XSPEC to assess the goodness of the fit: this command performs Monte Carlo simulations of spectra using the best-fitting model and gives the percentage of the simulated spectra that had a fit statistic less than that obtained from the fit to the real data. A value of 50 per cent is expected if the best-fitting model is a good representation of the data. Values much less than 50 per cent indicate that the data are overparameterized by the model since random statistical fluctuations in the majority of the simulated spectra are not able to produce a fit statistic as low as that obtained from the real data. In the opposite limit, when 100 per cent of the simulated spectra have a fit statistic less than that obtained from the real data, the fit is clearly poor. Column 6 in Table 2 shows that we obtained a goodness of 36.9 per cent, indicating that the data are still somewhat over-parameterized. The results for the width of the Fe K$\alpha$ line obtained from the *Chandra* HEG fit will be discussed in §4.3, along with the *Suzaku* constraints on the Fe K$\alpha$ line FWHM.

### 4.1 Intrinsic Continuum

In Table 2 it can be seen that the photon index of the hard power-law intrinsic continuum, $\Gamma_h$, is very similar for all four *Suzaku* fits, ranging from $1.895^{+0.016}_{-0.020}$ to $1.920^{+0.018}_{-0.024}$. Thus, $\Gamma_h$ is not sensitive to the assumed inclination angle of the torus, nor to the uncertainty in the PIN:XIS normalization ratio. The value of $\Gamma_h \sim 1.9$ for the intrinsic hard X-ray continuum is typical of type 1 AGN (e.g. Nandra et al. 2007; Dadina 2007 and references therein). The photon index of the soft continuum component, $\Gamma_s$, is much larger (and has larger fractional statistical errors), but is again similar for all four *Suzaku* fits, ranging from $6.88^{+1.54}_{-1.25}$ to $7.60^{+1.73}_{-1.24}$. The ratio of the normalization of the soft to hard continuum components, $r_{\rm PL}$, is also similar for all four *Suzaku* fits, ranging from $1.56^{+1.46}_{-0.62}$ to $1.88^{+2.19}_{-0.87}$. Note that for the *Suzaku* fit that used only the XIS data (column 5 in Table 2), $\Gamma_h$ and $r_{\rm PL}$ had to be fixed at their best-fitting values in order to derive the statistical errors on $\Gamma_s$, otherwise the fit became unstable. For the same reason, $\Gamma_s$ and $\Gamma_h$ had to be fixed at their best-fitting values in order to derive the statistical errors on $r_{\rm PL}$. This also explains why the statistical errors on $\Gamma_s$ and $r_{\rm PL}$ are relatively smaller for the XIS-only fit than for the joint XIS/PIN fits.

Although the values of $\Gamma_s$ appear to be unusually high, the soft X-ray power-law component only makes a significant

contribution to the continuum flux in a narrow bandpass of $\sim 1.5$ to 2 keV. The largest contribution is at 1.5 keV (the lowest energy of the fitted range), and even that is only $\sim 11$ per cent of the total continuum flux. This percentage can be calculated from the values of $r_{\rm PL}$, $\Gamma_s$, and $\Gamma_h$ given in Table 2. It can also be seen from Fig. 2 that the steepening of the continuum at low energies is barely noticeable. The lack of bandpass leverage combined with the weakness of the soft X-ray power law and small fluctuations due to calibration systematics, conspire to give a high value of $\Gamma_s$. If we extend the fitted bandpass down to 0.5 keV, smaller values of $\Gamma_s \sim 3.5$ are obtained. However, as described in §3, we did not use data below 1.5 keV for the full spectral analysis because there are larger systematic calibration uncertainties below 1.5 keV that manifest as discrepancies between the three XIS detectors that are larger than the statistical uncertainties in the data. Since the soft X-ray power-law continuum component is only an empirical parameterization, the value of $\Gamma_s$ obtained should not be interpreted as having any physical meaning.

### 4.2 X-ray Reprocessor Column Densities

Table 2 shows that the column density, $N_{\rm H}$, obtained from the baseline MYTORUS model, is $0.902^{+0.206}_{-0.216} \times 10^{24}$ cm$^{-2}$, which is nearly Compton thick. Formally, a Compton-thick medium is defined by an optical depth to electron scattering in the Thomson limit that is greater than unity, or $N_{\rm H} > (1.2\sigma_T)^{-1}$, or $N_{\rm H} > 1.25 \times 10^{24}$ cm$^{-2}$. The best-fitting value of $A_S$ for the baseline fit is $1.370^{+0.099}_{-0.086}$, implying that the global covering factor of the X-ray reprocessor may be greater than 50 per cent. The remaining three *Suzaku* spectral fits do show significant model dependences that affect the inferred values of $N_{\rm H}$. In the fit in which $C_{\rm PIN:XIS}$ is fixed at 1.16 (column 3, Table 2), $N_{\rm H}$ is $\sim 60$ per cent larger than the value obtained from the baseline fit (in which $C_{\rm PIN:XIS}$ was free). The value of $A_S$ is statistically consistent with that obtained from the baseline fit. In the *Suzaku* fit in which the torus inclination angle was fixed at 59° (column 4, Table 2), $N_{\rm H}$ is $\sim 11$ per cent smaller than the value obtained from the baseline fit (but the change is smaller than the statistical errors), whilst $A_S$ is $\sim 30$ per cent larger than the baseline value. Finally, in the *Suzaku* fit in which only the XIS data were utilized (column 5, Table 2), $N_{\rm H} = 1.00^{+3.00}_{-0.37}$, which is consistent with the value obtained from the baseline fit. The corresponding value of $A_S$ is also consistent with that from the baseline fit. In conclusion, the spectral fits give a consistent global column density if the $C_{\rm PIN:XIS}$ parameter is allowed to float, or if only the XIS data are used. In particular, both the baseline model fit, and the fit in which only the XIS data are used, are statistically consistent with $N_{\rm H} \sim 0.9 \times 10^{24}$ cm$^{-2}$. Both of these have face-on orientations of the torus, but other, non-grazing, orientations of the torus have little impact on this inferred column density. Table 2 shows that the nearly grazing inclination angle of 59° gives a value of $N_{\rm H}$ that is still statistically consistent with the baseline value. The derived value of $N_{\rm H}$ is controlled by several aspects of the observed spectrum working in tandem. The XIS-only fit shows that the lower limit on $N_{\rm H}$ is strongly controlled by the curvature in the spectrum between $\sim$ 4–10 keV together with the flux of the narrow Fe K$\alpha$ line. The high-energy continuum shape then controls the upper limit on $N_{\rm H}$ (a value that is too large would produce too much curvature).

### 4.3 Fe K$\alpha$, Fe K$\beta$ Emission Lines, and Fe K Edge

Table 2 shows that the best-fitting energy shift of the peak of the Fe K$\alpha$ line from the baseline model fit (column 2) is $20.0^{+7.9}_{-6.0}$ eV, and is likely a result of systematic effects in the XIS energy scale, and possibly mild ionisation. As far as Fe K$\alpha$ line fluorescence and Compton-reflection is concerned, this level of ionisation is negligible and does not conflict with the assumption that the X-ray reprocessor is essentially neutral. The other three *Suzaku* spectral fits give energy shifts consistent with that from the baseline model. The *Chandra* HEG fit also gives a consistent energy shift but the statistical errors are much larger.

From the baseline *Suzaku* fit (Table 2, column 2), the Fe K$\alpha$ line flux and EW were measured to be $3.14^{+0.23}_{-0.20} \times 10^{-5}$ photons cm$^{-2}$ s$^{-1}$, and $123^{+9}_{-8}$ eV respectively, where the EW was calculated with respect to the total continuum at the line peak (in the AGN frame). The Fe K$\alpha$ line flux and EW from the other three *Suzaku* fits, as well as from the *Chandra* HEG fit, are all consistent with the corresponding values from the baseline *Suzaku* fit.

The Fe K$\alpha$ line FWHM from the baseline *Suzaku* fit is $4475^{+1730}_{-2065}$ km s$^{-1}$, and similar values for the FWHM and statistical errors were obtained from the other three *Suzaku* fits (see Table 2). The *Chandra* HEG fit gave FWHM $= 3390^{+11350}_{-1040}$ km s$^{-1}$. Unfortunately, due to the limited signal-to-noise ratio of the HEG data, the FWHM has a lower limit that is similar to the *Suzaku* lower limit, and an upper limit which is worse than the upper limit measured from the *Suzaku* data. Although the one-parameter, 90 per cent confidence statistical errors imply that the Fe K$\alpha$ line is resolved in all cases, we found that joint, two-parameter confidence contours of the line peak energy shift versus line FWHM showed that at 99 per cent confidence the line is not resolved by either the *Suzaku* XIS nor the *Chandra* HEG. Nevertheless, it is clear that the Fe K$\alpha$ line could originate from the same location as the optical broad-line region (BLR) since the Fe K$\alpha$ line width measurements are consistent with the widths of some well-studied optical emission lines in Fairall 9. For example, for H$\beta$ ($\lambda$4861), FWHM $= 6901 \pm 707$ km s$^{-1}$ (Santos-Lieo et al. 1997), whilst for C IV($\lambda$1549) and Ly$\alpha$ ($\lambda$1216), FWHM $= 4628 \pm 1375$ and $3503 \pm 1474$ km s$^{-1}$ respectively (Rodriguez-Pascual et al. 1997).

Using the simple prescription of Netzer (1990) for relating the virialized velocity of matter orbiting a black hole to the location of the matter, the characteristic radius of the line-emitting region can be written $r \sim (4/3)(c/\mathrm{FWHM})^2 r_g$. Here, $r_g \equiv GM/c^2 = 1.5 \times 10^{13}\ M_8$ cm is the gravitational radius, where $M_8$ is the black-hole mass in units of $10^8\ M_\odot$. From the *Suzaku* FWHM measurements in Table 2, the largest upper limit is 6205 km s$^{-1}$ and the smallest lower limit is 1895 km s$^{-1}$ (the *Chandra* HEG lower limit is higher than this). These values correspond to a range in FWHM/$c$ of $6.32 \times 10^{-3}$ to $2.07 \times 10^{-2}$. This range corresponds to a spread in the distance of the Fe K$\alpha$ line emitter from the central black hole of 3112 to 33, 381 gravitational radii. This range in turn corresponds to a distance of 0.015 to 0.162 $M_8$ pc. Bentz & Katz (2015) have compiled a database of AGN black-hole measurements from BLR optical reverberation mapping campaigns[6] that includes Fairall 9. In addition to measurement errors, there is a large uncertainty in the mass derived from reverberation campaigns due to the unknown geometry of the line-emitting region. The compilation for Fairall 9 by Bentz & Katz (2015; see also Peterson et al. 2004) yields a range in the black hole mass of $M_8 = 0.99$ to 3.05. Taking into account this range in the black hole mass, the distance of the Fe K$\alpha$ line emitter from the black hole is then 0.015 to 0.49 pc.

The MYTORUS model self-consistently calculates the Compton shoulder of both the Fe K$\alpha$ and Fe K$\beta$ lines. A detailed study of the Fe K$\alpha$ line Compton shoulder in the MYTORUS model has been given in Yaqoob & Murphy (2011), and there it is shown that for $N_{\rm H} \sim 10^{24}$ cm$^{-2}$, and a face-on torus orientation, the flux in the Compton-shoulder is $\sim 25$ per cent of the unscattered line core. It can be seen from the model overlaid on the data in the Fe K region in Fig. 3(b), and the corresponding remarkably flat residuals in Fig. 3(d), that the fit to the entire Fe K region (including the Compton shoulder) is excellent. This is the case despite the fact that no empirical adjustments were applied to either of the Fe fluorescent lines relative to the Compton-scattered continuum, and that the Fe abundance was fixed at the solar value. For a given set of model parameters that determine the Compton-scattered continuum, the Fe fluorescent lines are completely determined. Not only is the Fe K$\alpha$ line profile well-fit, but also the Fe K$\beta$ line and the Fe K edge are accounted for very well by the model.

### 4.4 Fe XXV and Fe XXVI Emission Lines

The centroid energies of the (unresolved) Gaussian components used to model the ionised Fe emission lines were $6.752^{+0.038}_{-0.038}$ and $6.970^{+0.039}_{-0.032}$ keV from the *Suzaku* baseline model fit (see Table 2, column 2). We identified the lower and higher energy lines with Fe XXV(r) and Fe XXVI Ly$\alpha$ emission respectively. The expected energy for the Fe XXV(r) line is 6.700 keV[7], and that for the Fe XXVI Ly$\alpha$ line is 6.966 keV (Pike et al. 1996). It can be seen from Table 2 that the flux and equivalent width (EW) of the Fe XXV(r) line from the baseline *Suzaku* spectral fit are $0.43^{+0.15}_{-0.15} \times 10^{-5}$ photons cm$^{-2}$ s$^{-1}$ and $16.8^{+5.9}_{-5.9}$ eV respectively. The flux and EW of the Fe XXVI Ly$\alpha$ line, also from the baseline *Suzaku* fit, are $0.41^{+0.16}_{-0.16} \times 10^{-5}$ photons cm$^{-2}$ s$^{-1}$ and $18.5^{+7.2}_{-7.2}$ eV respectively. The flux and EW of both the Fe XXV(r) and Fe XXVI Ly$\alpha$ lines from the other three *Suzaku* spectral fits are all statistically consistent with the corresponding values obtained from the *Suzaku* baseline fit (Table 2). The signal-to-noise ratio of the *Chandra* HEG data was too poor to detect either of the two Fe emission lines so only upper limits on the fluxes and EWs are given in Table 2.

Narrow emission lines due to Fe XXV and Fe XXVI from highly ionised matter are common in both type 1 and type 2 AGN (e.g. see Yaqoob et al. 2003; Bianchi et al. 2005, 2009; Fukazawa et al. 2011; Patrick et al. 2013; Lobban & Vaughan 2014). Estimates on the frequency of occurrence of these emission lines vary. Whilst the frequency of occurrence of these emission lines has yet to be robustly established, recently, Patrick et al. 2013 estimated the fraction of sources with Fe XXV and Fe XXVI line emission in a sample of 46 type 1 AGN to be 52 and 39 per cent respectively. The ionised line-emitting matter must be located at a greater distance from the central engine than the putative torus but an X-ray spectral resolution better than the *Chandra* HEG is required to further tighten the constraints. The *Chandra* HEG resolution is $\sim 1780$ and 1710 km s$^{-1}$ FWHM at 6.7 and 6.966 keV respectively.

### 4.5 Fluxes and Luminosities

Continuum fluxes and luminosities obtained from all the spectral fits are shown in Table 2 for the 2–10 keV band, and for the 10–30 keV energy bands for the *Suzaku* fits. For fluxes, these energy bands are in the observed frame, but for luminosities, the lower and upper energies in each band are quantities in the source frame, so that they appear redshifted in the observed frame. For regions where there were no data, the models were extrapolated. Two luminosities are given for each band, one set ($L_{\rm obs}$) was derived directly from the best-fitting model, and the second set, $L_{\rm intr}$, or intrinsic luminosity, was derived by removing all absorbing and reflecting model components.

The 2–10 keV observed fluxes are similar for all four *Suzaku* spectral fits, lying in the range 2.31 to $2.35 \times 10^{-11}$ erg cm$^{-2}$ s$^{-1}$. The chandra HEG 2–10 keV flux is $2.11 \times 10^{-11}$ erg cm$^{-2}$ s$^{-1}$. The observed 2–10 keV luminosity is $\sim 1.2 \times 10^{44}$ erg s$^{-1}$ for

[6] http://www.astro.gsu.edu/AGNmass/
[7] http://physics.nist.gov/PhysRefData

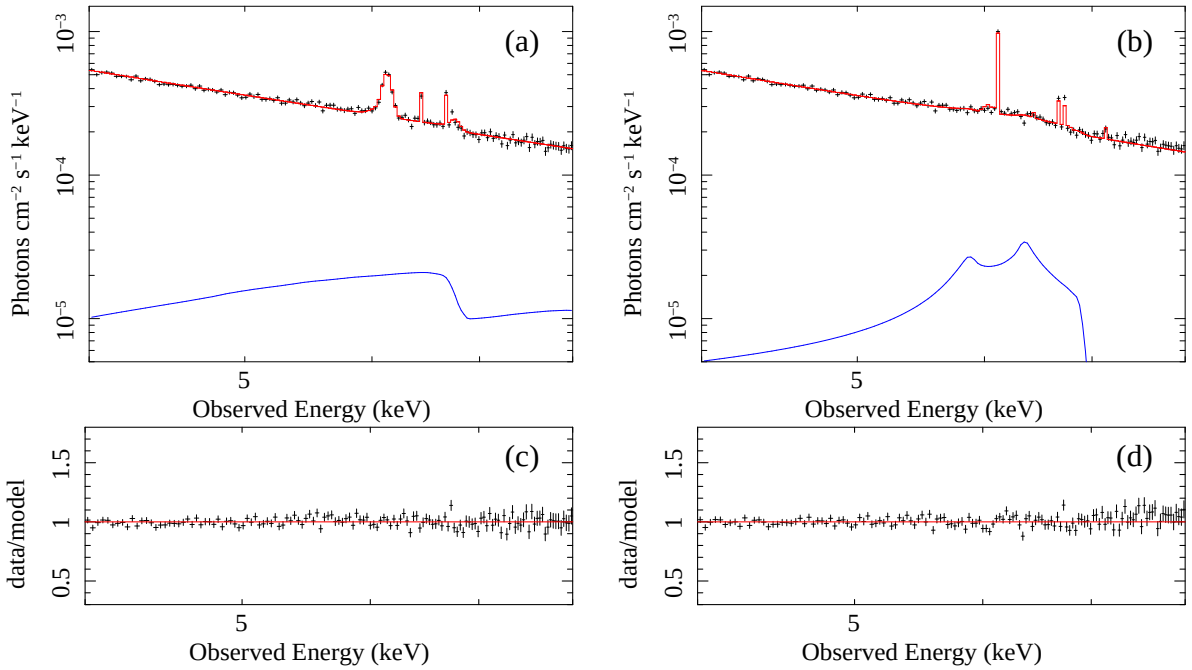



**Figure 5.** A comparison, in the 4–8 keV band, of the best-fitting baseline face-on MYTORUS fit with a "blurred reflection" model, similar to that fitted type fitted by Lohfink et al. (2012a), showing how the MYTORUS model can eliminate the need for a relativistically broadened Fe K$\alpha$ line. Both models include narrow Fe XXV and Fe XXVI Ly$\alpha$ emission lines from distant ionised material (but the fitted Fe XXV flux for the blurred reflection model is negligible). (a) Unfolded photon spectrum (black) overlaid with the total MYTORUS model (red; see Table 2, column 2). The Compton-scattered continuum from the MYTORUS model shown in blue is able to account for excess emission in the Fe K band instead of a relativistically broadened Fe K$\alpha$ line. (b) Unfolded photon spectrum (black) overlaid with the total multi-component Lohfink et al. (2012a) disc reflection and Comptonisation model in red (see text for details). The blurred reflection component is shown in blue. Above the blue wing of the relativistic Fe K$\alpha$ line, the reflection continuum drops by more than an order of magnitude but rises again at high energies. Note that in this model fit, the narrow Fe K$\alpha$ is unresolved because Lohfink et al. (2012a) did not include any broadening for this component. Panels (c) and (d) show the data to model ratios corresponding to (a) and (b) respectively, showing that both models give good fits to the data. Note that, although the MYTORUS component and blurred reflection component (shown in blue in panels (a) and (b) respectively) appear to be markedly different from each other, smearing due to the limited CCD detector energy resolution has a considerable impact on the ability of the data to distinguish between the two models. This is illustrated in Fig. 6. (A color version of this figure is available in the online journal.)

the *Suzaku* fits, and $\sim 1.1\times10^{44}$ erg s$^{-1}$ for the *Chandra* HEG fit. The intrinsic 2–10 keV luminosities are very similar to each other for all of the spectral fits, since the 2–10 keV band is dominated by the intrinsic continuum. The 10–30 keV fluxes are in the range $2.09-2.33\times10^{-11}$ erg cm$^{-2}$ s$^{-1}$ for the four *Suzaku* fits, and the corresponding observed 10–30 keV luminosities are in the range 1.08–1.20 $\times\,10^{44}$ erg s$^{-1}$. The intrinsic 10–30 keV luminosities are in the range $0.87-0.90\times10^{44}$ erg s$^{-1}$, somewhat less than the observed luminosities, because the latter include reflection from the torus which increases the apparent luminosity. Note that the intrinsic 10–30 keV luminosities were derived using the XIS normalizations, so they do not include the effect of different values of the PIN:XIS normalization ratio (which does, however, affect the observed luminosities).

### 4.6 HXD/PIN Background Subtraction Systematics

In this section we evaluate the effect of a $\pm1$ per cent error in the HXD-PIN background subtraction on the key parameters of the baseline MYTORUS *Suzaku* model fit (Table 2, column 2). Both scenarios did not significantly change the quality of the fit, with $\Delta\chi^2<1$ for both cases. Moreover, the effect on continuum fluxes for both cases was negligible. Compared to the baseline fit values, the 2–10 keV fluxes and the 10–30 keV fluxes changed by $<2$ per cent. On the other hand, we found that changing the background by +1 per cent gave $N_{\rm H}=0.895^{+0.456}_{-0.341}\times10^{24}$ cm$^{-2}$, $\Gamma=1.905^{+0.019}_{-0.020}$, $A_S=1.377^{+0.170}_{-0.091}$, and $C_{\rm PIN:XIS}=1.26^{+0.102}_{-0.105}$. Changing the background by $-1$ per cent gave $N_{\rm H}=0.894^{+0.338}_{-0.495}\times10^{24}$ cm$^{-2}$, $\Gamma=1.905^{+0.018}_{-0.021}$, $A_S=1.375^{+0.167}_{-0.090}$, and $C_{\rm PIN:XIS}=1.390^{+0.109}_{-0.111}$. Thus, compared to the corresponding values with standard background in Table 2, column 2, only the value of $C_{\rm PIN:XIS}$ is impacted and there is no statistically significant change to the other parameters. In the case that the background is changed by +1 per cent, the value of $C_{\rm PIN:XIS}$ becomes consistent with the "recommended value" of 1.16 for XIS-nominal observations. We note that the background-subtraction systematics cannot be completely described by a single number and in reality have an energy dependence. Also, they are largest between $\sim$ 10–20 keV, and the residuals as a function of energy, obtained when the model is applied to different Earth occultation data sets,

are not identical[8]. The pattern of the PIN residuals in the fit with $C_{\rm PIN:XIS}$ fixed at 1.16 (Fig. 3(e)) could be the result of the limitations of the background model. Thus, the value of $C_{\rm PIN:XIS} = 1.32 \pm 0.11$ from the baseline fit does not appear to be too unreasonable.

### 4.7 Comparison with Relativistic Line Models

In this section we investigate how the Compton-scattered continuum in the MYTORUS fits to the Fairall 9 *Suzaku* data is able to mimic a relativistically broadened Fe K$\alpha$ line by directly comparing the face-on MYTORUS fit with a so-called "blurred reflection" model fitted by Lohfink et al. (2012a) to the same data. We do not delve in detail into fitting ionised accretion disc models with relativistic blurring because such model fits with several variations on the basic theme have been described at length in Lohfink et al. (2012a) and there is little to gain from repeating the analysis. Instead, we take one of the preferred models of Lohfink et al. (2012a) and directly compare the shape of the blurred reflection spectrum, which includes the relativistic Fe K$\alpha$ line, with the component of the MYTORUS model that replaces the relativistic emission. Specifically, we adopt the blurred reflection model fit shown in Table 4 (under the "*Suzaku A*" column) in Lohfink et al. (2012a). This is one of the two preferred models from multi-epoch fitting in that work, and has one ionised reflection component, whereas the other model is more complicated and has two ionised reflection components. The ionised reflection is modeled with the REFLIONX model, and this is convolved with the model RELCONV to implement the relativistic blurring. The Lohfink et al. (2012a) fit employs additional model components, namely PEXMON for the narrow, distant-matter Fe K$\alpha$ line and reflection continuum; COMPTT for a Comptonisation continuum; and an XSTAR table for an ionised plasma component. However, we did not include the latter because it is relatively weak and does not impact the fitted reflection or other continuum components. Although the Fe XXV and Fe XXVI emission lines are also relatively weak, we modeled them with individual, unresolved Gaussian components, as was done for the MYTORUS fits described in §4, allowing only the centroid energies and line fluxes to be free parameters. We froze the parameters of the remaining model components at the values in Table 4 of Lohfink et al. (2012a), including $C_{\rm PIN:XIS} = 1.16$, except for the normalizations of continuum components, and fitted the model to the same *Suzaku* XIS and PIN spectra that were used for fitting the MYTORUS model. Specifically, the power-law photon index was $\Gamma = 1.90$, the distant-matter reflection fraction for PEXMON was 0.84, the disc ionisation parameter was $\xi = 10.1$, the disc inclination angle was 48°, the radial emissivity index was $q = 2.0$, the iron abundance in the REFLIONX model relative to solar was 10.0, and the black-hole spin was $a = 0.52$. The temperature of the Comptonisation component was $kT = 20.52$ keV, and the optical depth of the Comptonising matter was $\tau = 0.52$.

In Fig. 5(a) and Fig. 5(b) we compare, in the critical 4–8 keV band, the unfolded spectra for the face-on MYTORUS fit and for the blurred reflection model respectively. The data to model ratios are shown in Fig. 5(c) and Fig. 5(d), from which it can be seen that neither model leaves significant residuals. For the blurred reflection model we obtained $\chi^2 = 368.0$ for 244 degrees of freedom, corresponding to a reduced $\chi^2$ value of 1.508 and null hypothesis probability of $4.8 \times 10^{-7}$. However, it is principally the residuals at energies below $\sim 3$ keV that are responsible for the high value of $\chi^2$ since we did not include the photoionised plasma component. We note that Lohfink et al. (2012a) give $\chi^2 = 2232.6$ for 2095 degrees of freedom, or a reduced $\chi^2$ value of 1.066 (null hypothesis probability of 0.02), for the full blurred reflection model that they fitted, which did include the photoionised plasma emission. However, there are additional differences between our blurred reflection model fit and that of Lohfink et al. (2012a). One is that the latter used two separate XIS spectra (one combining XIS0 and XIS3 data, the other corresponding to XIS1 data only). In addition, Lohfink et al. (2012a) employed a different energy band for fitting the PIN data, namely 16–35 keV, as opposed 12.5–42.5 keV, and they used XIS data up to 10 keV. When we repeated our blurred reflection model fit with data below 3 keV excluded, using two separate XIS spectra as described, and the same energy ranges as Lohfink et al. (2012a), we obtained a reduced $\chi^2$ value of 1.099 (null hypothesis probability of 0.065). Considering the fact that our data selection criteria and extraction regions for XIS source and background data are not completely identical, we conclude that our blurred reflection fit results are consistent with those of Lohfink et al. (2012a). The blurred reflection model fitted by Lohfink et al. (2012a) and the MYTORUS model fit (see Table 2) give reduced $\chi^2$ values that are comparable, which indicates that the two model fits are statistically similar to each other. In our blurred reflection model fit described above, the value of $C_{\rm PIN:XIS}$ was fixed at 1.16, as it was in Lohfink et al. (2012a). When we allowed $C_{\rm PIN:XIS}$ to be a free parameter, the value of $\chi^2$ dropped by only 1.6, and we obtained $C_{\rm PIN:XIS} = 1.10^{+0.08}_{-0.08}$, which encompasses the value of 1.16.

The model components in blue in Fig. 5(a) and Fig. 5(b) show how the Compton-scattered continuum from the MYTORUS model and the relativistically broadened Fe K$\alpha$ line with blurred disc continuum respectively provide very different solutions to the same data. At a disc inclination angle of 48°, the relativistic line has significant emission in the blue wing but it also has a trailing red wing. In the MYTORUS model, the downturn at low energies of the Compton-scattered continuum, combined with the Fe K edge in that continuum conspire to mimic the relativistic line in the blurred reflection model. Note that in the blurred reflection model the reflection continuum above the blue wing of the broad Fe K$\alpha$ line drops by more than

[8] ftp://legacy.gsfc.nasa.gov/suzaku/doc/hxd/suzakumemo-2008-03.pdf

order of magnitude but recovers again at higher energies (see plots in Lohfink et al. 2012a). Obviously, if the data had better spectral resolution, the two models may be distinguishable, but at CCD spectral resolution they are not distinguishable (this is demonstrated in Fig. 6, discussed below). It is also important to note that it can be seen that the Compton-shoulder in the MYTORUS model fit is not the reason why the MYTORUS model is able to mimic the relativistic line in Fairall 9, in part because the shoulder cannot explain the blue wing, but also because with the velocity broadening of the narrow Fe K$\alpha$ line of $\sim 4475^{+1730}_{-2065}$ km s$^{-1}$ FWHM (see Table 2), the Compton shoulder cannot be discerned as a distinct feature. This is expected, especially for data with CCD spectral resolution (see Yaqoob & Murphy 2011 for a detailed discussion). The velocity broadening of the narrow, distant-matter Fe K$\alpha$ line highlights another important difference between the MYTORUS and blurred reflection model fits. Lohfink et al. (2012a) did not apply velocity broadening to the distant-matter Fe K$\alpha$ line, which is part of the PEXMON model in their blurred reflection fit. No justification was given for this omission, so it is an implicit assumption of their model that the line-emitting matter is sufficiently far from the central mass that Doppler broadening is negligible compared to the CCD energy resolution. The result of this assumption is that the relativistic line in the blurred reflection model partly models the distant-matter narrow Fe K$\alpha$ line, thereby exaggerating the relative importance of the relativistic line. This is illustrated in Fig. 6: the counts spectra overlaid with the MYTORUS and blurred reflection models are shown in Fig. 6(a) and Fig. 6(b) respectively, which in turn correspond to the same fits shown against the unfolded spectra in Fig. 5(a) and Fig. 5(b) respectively. The result of turning off the Compton-scattered continuum in the MYTORUS model is then shown in Fig. 6(c), whilst the result of turning off the blurred reflection component in the Lohfink et al. (2012a) fit is shown in Fig. 6(d). In the latter, it can be seen that turning off the relativistic Fe K$\alpha$ line in the model leaves an excess in the data on blue side of the distant-matter Fe K$\alpha$ line. This is not the case for MYTORUS model. The data to model ratios corresponding to Fig. 6(c) and Fig. 6(d) are shown in Fig. 6(e) and Fig. 6(f) respectively (note that the ratios are binned by a factor of 4 for clarity compared to the spectral plots). The data to model ratios further confirm that the broad, relativistic Fe K$\alpha$ line is modeling part of the narrow, distant-matter Fe K$\alpha$ line, and that aside from this difference, the feature in Fig. 6(e) modeled by the MYTORUS model Compton-scattered continuum is, as expected, very similar to the broad feature modeled as a relativistic line in Fig. 6(f). Whilst the limited signal-to-noise ratio of the data plays a role in allowing both models to fit the data, the smearing due to the limited energy resolution of CCD data is a key factor. If the energy resolution were better, the data to model ratios in Fig. 6(e) and Fig. 6(f), which by definition have the models folded through the instrument response function, would reflect more clearly the differences in spectral shape between the two different models of the broad spectral feature.

Whereas the above analysis considered the MYTORUS and blurred reflection models separately, next we consider the upper limit on a blurred reflection model when it is added to the baseline MYTORUS model (Table 2, column 2). Since it is clear from the residuals to the MYTORUS model (e.g., Fig. 3(d)) that adding a relativistic Fe K$\alpha$ line would essentially result in fitting the noise in the data, the question of an upper limit on a blurred reflection component must be posed in a very specific context in order to give a meaningful result. Allowing too many free parameters may result in none of them being constrained. Thus, we added a REFLIONX model component, convolved with the RELCONV model, and again tested against the best-fitting values of the parameters given in Table 4 of Lohfink et al. (2012a), fixing those parameters in the fits, except for the normalization of the REFLIONX component. We then obtained the 1-parameter, 90 per cent confidence upper limit on this normalization. The upper limit that we obtained corresponds to a 2–10 keV flux for the blurred reflection component that is only 1.2 per cent of the total 2–10 keV flux.

In the REFLIONX model, the Fe K$\alpha$ line from the disc cannot be separated from the disc-reflection continuum, so the equivalent width (EW) of the Fe K$\alpha$ cannot easily be calculated. Therefore, we also considered the upper limit on the EW of a relativistically broadened Fe K$\alpha$ line that is not attached to a reflection continuum, when it is added to the baseline MYTORUS model fit. Inclusion of a reflection continuum would only reduce the upper limit on the EW. We tested the data against the LAOR model which gives a line profile due to emission from a disc associated with a maximally spinning black hole ($a = 0.998$; see Laor 1991). We fixed the inner disc radius at a value appropriate for the spin, namely 1.235 gravitational radii, and we fixed the outer disc radius at 400 gravitational radii. We also fixed the radial emissivity index at 2.0. The disc inclination angle was fixed at the value of 48° (i.e. the value in Table 4 of Lohfink et al. 2012a). We obtained a 1-parameter, 90 per cent upper limit on the EW of 27 eV. We repeated the procedure with the inclination angle fixed at 0° and again obtained a small upper limit on the EW of the relativistic line of 32 eV. Using line profiles corresponding to smaller values of black-hole spin would result in even smaller upper limits on the EW because the innermost stable orbit radius increases with decreasing black-hole spin, so the corresponding line profiles would have decreasing width.

## 5 SUMMARY

We have re-analysed *Suzaku* data for the "bare" Seyfert 1 galaxy, Fairall 9, applying the MYTORUS model of Murphy & Yaqoob (2009) that self-consistently calculates the Fe K$\alpha$ line emission and X-ray reflection spectrum from a toroidal distribution of neutral matter with solar iron abundance. We find that an excellent fit is obtained for the detailed Fe K$\alpha$

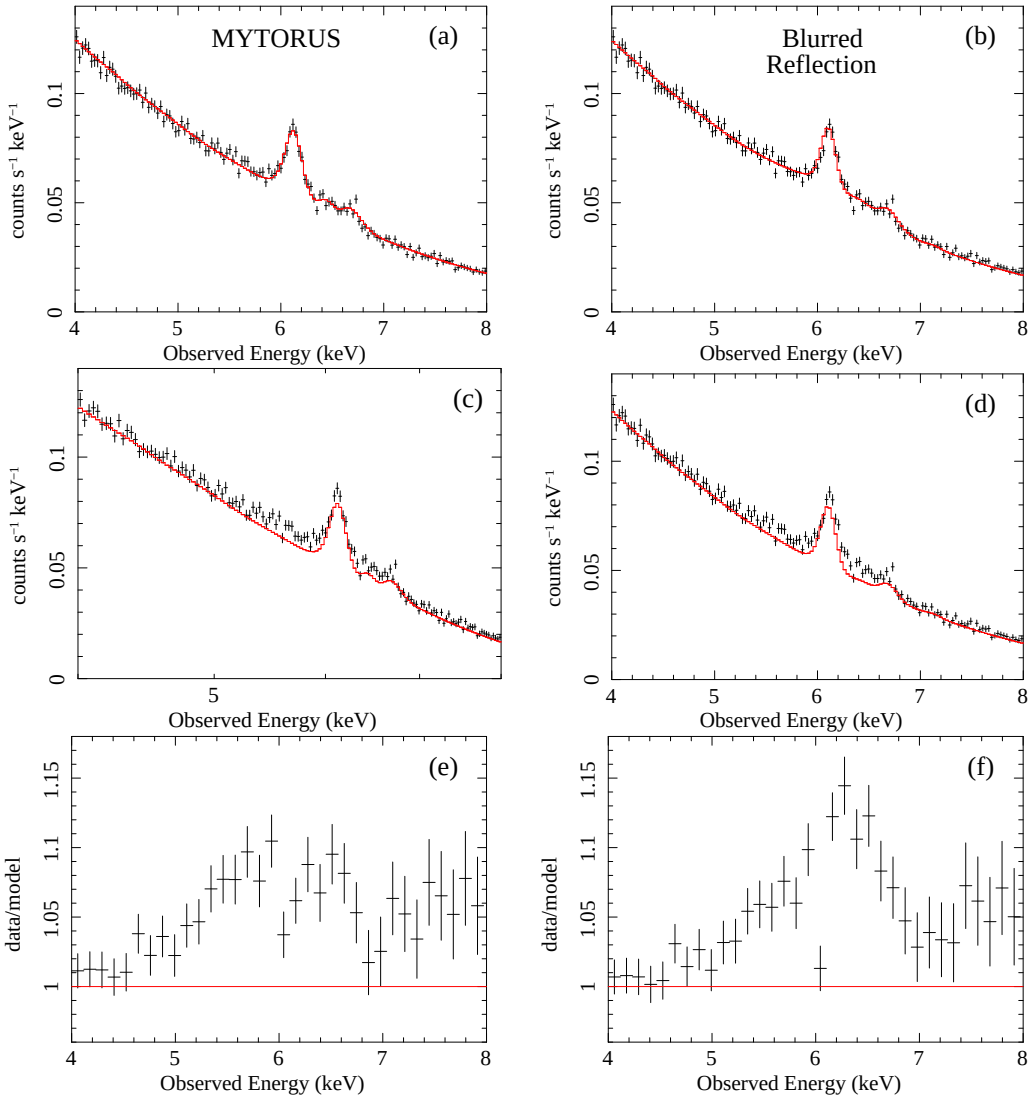



**Figure 6.** The effect of turning off the Compton-scattered continuum in the best-fitting baseline face-on MYTORUS model, compared with turning off the reflection component (which includes the relativistically broadened Fe K$\alpha$ line) in the blurred reflection model (see text for details). (a) XIS counts spectrum of Fairall 9 (black), overlaid with the best-fitting face-on MYTORUS (red; see Table 2, column 2). (b) XIS counts spectrum of Fairall 9 (black), overlaid with the blurred reflection model, similar to that fitted by Lohfink et al. (2012a), and described in §4.7. (c) As (a) but with the Compton-scattered continuum in the MYTORUS model turned off. (d) As (b) but with the blurred reflection component turned off. Panels (e) and (f) show data to model ratios corresponding to (c) and (d) respectively. In the blurred reflection fit, the distant-matter, narrow Fe K$\alpha$ is unresolved because Lohfink et al. (2012a) did not allow it to be free. It can be seen that consequently, the relativistic Fe K$\alpha$ line in the blurred reflection model is actually modeling part of the the narrow Fe K$\alpha$ line. Otherwise, the feature in (e) modeled by the Compton-scattered continuum of the MYTORUS model is, as expected, very similar to the broad feature in (f) modeled as a relativistic line. Note that for clarity, the data/model ratios are binned by a factor of 4 compared to the spectral plots. (A color version of this figure is available in the online journal.)

line profile including the red and blue wings, the Fe K$\beta$ line, the Fe K edge, and the "Compton hump" associated with the X-ray reflection spectrum. The same best-fitting parameters that determine the magnitude and shape of the X-ray reflection continuum also determine the Fe K$\alpha$ line flux and profile with no additional freedom. The data require no ad hoc adjustment or interference of this self-consistency. We obtained an equatorial column density of the toroidal X-ray reprocessor of $N_{\rm H} = 0.902^{+0.206}_{-0.216} \times 10^{24}$ cm$^{-2}$ from a baseline fit, for the case that the torus is observed face-on and the cross-normalization between the PIN and XIS data is allowed to be free. Other lines of sight that do not intercept the torus also provide excellent fits to the data, yielding similar constraints on the column density. A face-on fit with the PIN data removed altogether also provides consistent constraints on $N_{\rm H}$. On the other hand, fixing the cross-normalization between the PIN and XIS spectra at the default value gives a column density that is $\sim 60$ per cent higher than that from the baseline fit.

The baseline, face-on toroidal model gives a velocity broadening of the Fe K$\alpha$ line of $4475^{+1730}_{-2065}$ km s$^{-1}$ FWHM. Variations on the baseline model also gave consistent values for the FWHM of the Fe K$\alpha$ line. The FWHM measured here does not

confuse broadening due to the Compton shoulder of the Fe K$\alpha$ line with velocity broadening since the broadening due to the Compton shoulder is self-consistently modeled. The Fe K$\alpha$ line width places the distance of the X-ray reprocessor at $\sim 3.1$ to $33.4 \times 10^3$ gravitational radii from the putative central black hole. This corresponds to $\sim 0.015$ to 0.49 pc for a black-hole mass in the range $0.99 - 3.05 \times 10^8$ $M_{\odot}$ (from historical reverberation measurements). The statistical errors quoted here for the FWHM are for one parameter, 90 per cent confidence, but we found that the Fe K$\alpha$ line is not resolved at a confidence level of 99 per cent, for two parameters. Thus, a location for the Fe K$\alpha$ line emitter that is further out than $\sim 0.5$ pc cannot be ruled out. We also detected narrow, unresolved Fe XXV(r) and Fe XXVI Ly$\alpha$ emission lines from highly ionised matter in a region distinct from the Fe K$\alpha$ line emitter, further out from the central engine.

The MYTORUS models, using only mundane, nonrelativistic physics, give such good fits to the Fairall 9 data using only narrow Fe K$\alpha$ line emission and X-ray reflection from distant matter that there is no need for any more complexity in the models. In contrast, previous analyses of the same *Suzaku* data for Fairall 9 have applied relativistic disc-reflection models that produce broad Fe K$\alpha$ line emission and X-ray reflection from within a few gravitational radii of the black hole (Lohfink et al. 2012a, and references therein). Such fits have been used to directly derive constraints on the black-hole spin, or angular momentum. In our interpretation of the data, there are no signatures in the X-ray spectrum of the strong gravity regime, no broad Fe K$\alpha$ line, and therefore no measure of black-hole spin based on the Fe K$\alpha$ line and reflection spectrum. From a theoretical perspective, there is actually no precedent for emission features from within a few gravitational radii of the black hole to leave imprints on the X-ray spectrum since there are several ways to suppress such features. For example, the inner accretion disc may be truncated, or it may be too highly ionised (e.g. see Patrick et al. 2013 for a recent discussion). We showed in detail how the spectral shape of the MYTORUS model in the Fe K band is able to replace the relativistically broadened Fe K$\alpha$ line, but we also obtained an upper limit to the magnitude of a relativistically blurred accretion disc-reflection spectrum if it is included in addition to the MYTORUS model. Relative to the baseline MYTORUS model, the 2–10 keV flux in the blurred reflection spectrum is $< 1.2$ per cent of the total observed 2–10 keV flux.

An important factor in our MYTORUS spectral fits is the break from the common assumption that the X-ray reflector and fluorescent line emitter has an infinite column density. The X-ray reflection continuum from matter with a finite column density has a greater variety of spectral shapes than that from matter with an infinite column density. In particular, reflection spectra from matter with a finite column density can produce spectral structure around the Fe K$\alpha$ line that might otherwise be interpreted as the effects of relativistic smearing. Moreover, we note that in previous analyses of the X-ray spectra of Fairall 9 that derived black-hole spin measurements, the infinite column density disc model was not only applied to what was thought to be the relativistic components, but it was also used to model the distant-matter (narrow) Fe K$\alpha$ line and reflection spectrum. In future work we will apply the finite column density reprocessor models described here to other AGN and other observations of Fairall 9 in order to investigate whether our conclusions have a broader relevance.

Acknowledgments

The authors thank the anonymous referee for helping to improve the paper. The authors acknowledge support for this work from NASA grants NNX09AD01G, NNX10AE83G, and NNX14AE62G. This research has made use of data and software provided by the High Energy Astrophysics Science Archive Research Center (HEASARC), which is a service of the Astrophysics Science Division at NASA/GSFC and the High Energy Astrophysics Division of the Smithsonian Astrophysical Observatory.

This paper has been produced using the Royal Astronomical Society/Blackwell Science LaTeX style file.

## REFERENCES

Anders E., Grevesse N., 1989, Geochimica et Cosmochimica Acta 53, 197
Antonucci R. R. J., 1993, ARA&A, 31, 473
Arnaud K. A., 1996, in Astronomical Data Analysis Software and Systems V, ed. Jacoby, G., Barnes, J. (Astronomical Society of the Pacific), Conference Series, Vol. 101, p. 17
Bentz M. C., Katz S., 2015, PASP, 127, 67
Bianchi S., Bonilla N. F., Guainazzi M., Matt G., Ponti G., 2009, A&A, 501, 915
Bianchi S., Miniutti G., Fabian A. C., Iwasawa K., 2005, MNRAS, 360, 380
Brenneman L. W., Reynolds C. S., 2006, ApJ, 652, 1028
Brightman M., Nandra K., 2011, MNRAS, 413, 1206
Dadina M., 2007, A&A, 461, 1209
Dauser T., Wilms J., Reynolds C. S., Brenneman L., 2010, MNRAS, 409, 1534
Dovčiak M., Karas V., Yaqoob T., 2004, ApJS, 153, 205
Emmanoulopoulos D., Papadakis I. E., McHardy I. M., Nicastro F., Bianchi S., Arévalo P., 2011, MNRAS, 415, 1895
Fukazawa Y., et al., 2011, ApJ, 727, 19
Furui S., Fukazawa Y., Odaka H., Kawaguchi T., Ohno M., Hayashi K., 2016, ApJ, 818
Gallo L. C., et al., 2015, MNRAS, 446, 633
Gondoin P., Lumb D., Siddiqui H., Guainazzi M., Schartel N., 2001, A&A, 373, 806
Guainazzi M., La Parola V., Miniutti G., Segreto A., Longinotti A. L. 2012, A&A, 547, 31

Hagino K., Odaka H., Done C., Tomaru R., Watanabe S., Takahashi T. 2016, MNRAS, in press (arXiv:1509.05645v2)
Ikeda S., Awaki H., Terashima Y., 2009, ApJ, 692, 608
Ishisaki Y. et al., 2007, PASJ, 59, S113
Iso N., Ebisawa K., Sameshima H., Mizumoto M., Miyakawa T., Inoue H., Yamasaki H., 2016, PASJ, 68, 27
Kalberla P. M. W., Burton W. B., Hartmann D., Arnal E. M., Bajaja E., Morras R., Pöppel W. G. L., 2005, A&A, 440, 775
Koyama K., et al., 2007, PASJ, 59, 23
LaMassa S. M., Yaqoob T., Ptak A., Jianjun J., Heckman T. M., Gandhi P., Urry C. M., 2014, ApJ, 787, 61
Laor A., 1991, ApJ, 376, 90
Liu Y., Li X., 2014, ApJ, 787, 52
Liu Y., Li X., 2015, MNRAS, 448, L53
Lobban A. P., Vaughan S., 2014, MNRAS, 439, 1575
Lohfink A. M., Reynolds C. S., Miller J. M., Brenneman L. W., Mushotzky R. F., Nowak M. A., Fabian A. C., 2012a, ApJ, 758, 67
Lohfink A. M., Reynolds C. S., Mushotzky R. F., Wilms J., 2012b, ApJL, 749, L31
Lohfink A. M., et al. 2016, ApJ, 821, 11
Magdziarz P., Zdziarski A. A., 1995, MNRAS, 273, 837
Matt G., Guainazzi M., Maiolino R., 2003, MNRAS, 342, 422
Middleton M., 2015, in "Astrophysics of Black Holes - From fundamental aspects to latest developments", Ed. Cosimo Bambi, Springer: Astrophysics and Space Science Library, arXiv:1507.06153
Middleton M., Done C., Gierliński M., 2007, MNRAS, 381, 1426
Miller L., Turner T. J., Reeves J. N., 2008, A&A, 483, 437
Mitsuda K. et al., 2007, PASJ, 59, 1
Murphy K. D., Yaqoob T., 2009, MNRAS, 397, 1549
Nandra K., 2006, MNRAS, 368, L62
Nandra K., O'Neill P. M., George I. M., Reeves J. N., 2007, MNRAS, 382, 194
Netzer H. 1990, in Active Galactic Nuclei, ed. R. D. Blandford, H. Netzer, L. Woltjer (Berlin: Springer), 137
Nowak M. A., et al. 2011, ApJ, 728, 13
Patrick A. R., Reeves J. N., Lobban A. P., Porquet D., Markowitz A. G., 2011a, MNRAS, 416, 2725
Patrick A. R., Reeves J. N., Porquet D., Markowitz A. G., Braito V., Lobban A. P., 2013, MNRAS, 426, 2522
Patrick A. R., Reeves J. N., Porquet D., Markowitz A. G., Lobban A. P., Terashima Y., 2011b, MNRAS, 411, 2353
Peterson B. M., et al., 2004, ApJ, 613, 682
Pike C. D., et al. 1996, ApJ, 464, 487
Reynolds C. S., 1997, MNRAS, 286, 513
Reynolds C. S., 2014, SSRv, 183, 277
Ricci C., Ueda Y., Paltani S., Ichikawa K., Ghandi P., Awaki H., 2014, MNRAS, 441, 3622
Risaliti G., Elvis M., Bianchi S., Matt G., 2010, MNRAS, 406, L20
Rodríguez-Pascual P. M., 1997, ApJS, 110, 9
Ross R. R., Fabian A. C., 1995, MNRAS, 358, 211
Ross R. R., Fabian A. C., Young A., 1999, MNRAS, 306, 461
Santos-Lleó et al., 1997, ApJS, 112, 271
Schmoll S., 2009, ApJ, 703, 2171
Shu X. W., Yaqoob T., Wang J. X., 2010, ApJS, 187, 581
Shu X. W., Yaqoob T., Wang J. X., 2011, ApJ, 738, 147
Serlemitsos P. J. et al., 2007, PASJ, 59, 9
Sobolewska M. A., Done C., 2007, MNRAS, 374, 150
Sulentic J. W., Marziani P., Zwitter T., Calvani M., Dultzin-Hacyan D., 1998, ApJ, 501, 54
Takahashi T., et al., 2007, PASJ, 59, 35
Tatum M. M., Turner T. J., Sim S. A., Miller L., Reeves J. N., Patrick A. R., Long K. S., 2012, ApJ, 752, 94
Thorne K. S., 1974, ApJ, 191, 507
Urry C. M., Padovani P., 1995, PASP, 107, 803
Verner D. A., Ferland G. J., Korista K. T., Yakovlev D. G., 1996, ApJ, 465, 487
Volonteri M., Begelman M. C., 2010, MNRAS, 409, 1022
Walton D. J., Nardini E., Fabian A. C., Gallo L. C., Reis R. C., 2013, MNRAS, 428, 2901
Wilms J., Nowak M. A., Pottschmidt K., Pooley G. G., Fritz S., 2006, A&A, 447, 245
Yaqoob T., 2012, MNRAS, 423, 3360
Yaqoob T., George I. M., Kallman T. R., Padmanabhan U., Weaver K. A., Turner T. J. 2003, ApJ, 596, 85
Yaqoob T., Murphy K. D., 2011, MNRAS, 412, 277
Yaqoob T., Padmanabhan U., 2004, ApJ, 604, 63
Yaqoob T., Tatum M. M., Scholtes A., Gottlieb A., Turner T. J., 2015, MNRAS, 454, 973